Tectonophysics 623 (2014) 147–168

Contents lists available at ScienceDirect

Tectonophysics

journal homepage: www.elsevier.com/locate/tecto

Hydrothermal alteration in an exhumed crustal fault zone: Testing geochemical mobility in the Caleta Coloso Fault, Atacama Fault System, Northern Chile

Gloria Arancibia [a,b,*], Kazuna Fujita [c,1], Kenichi Hoshino [c], Thomas M. Mitchell [d,2], José Cembrano [a,b], Rodrigo Gomila [a,b], Diego Morata [b,e], Daniel R. Faulkner [f], Marieke Rempe [d,3]

[a] Department of Structural and Geotechnical Engineering, Pontificia Universidad Catolica de Chile, Avenida Vicuña Mackenna 4860, Macul, Santiago, Chile
[b] Andean Geothermal Centre of Excellence (CEGA, FONDAP-CONICYT), Plaza Ercilla 803, Santiago, Chile
[c] Department of Earth and Planetary Systems Science, Graduate School of Science, Hiroshima University, 1-3-1, Kagami-yama, Higashi-Hiroshima 739-8526, Japan
[d] Institut für Geologie, Mineralogie und Geophysik, Ruhr-Universität Bochum, Bochum, Germany
[e] Department of Geology, Universidad de Chile, Plaza Ercilla 803, Santiago, Chile
[f] Rock Deformation Laboratory, Department of Earth and Ocean Sciences, University of Liverpool, United Kingdom

ARTICLE INFO

Article history:
Received 19 August 2013
Received in revised form 20 March 2014
Accepted 24 March 2014
Available online 5 April 2014

Keywords:
Fault zone
Hydrothermal alteration
Mass balance
Chemical mobility

ABSTRACT

Crustal scale strike slip fault zones have complex and heterogeneous permeability structures, playing an important role in fluid migration in the crust. Exhumed faults provide insights into the interplay among deformation mechanisms, fluid–rock interactions and bulk chemical redistributions. We determined the whole-rock geochemistry and mineral chemistry of the fault core of the Caleta Coloso Fault in Northern Chile, in order to constrain the physical and chemical conditions that lead to strong hydrothermal alteration. The strike-slip Caleta Coloso Fault core has a multiple-core architecture, consisting of alternate low strain rocks (protolith, weakly deformed protolith and protocataclasites) and high-strain strands (cataclasites and discrete band of ultracataclasite) derived from a Jurassic tonalite. Hydrothermal alteration associated with fault-related fluid flow is characterized by a very low-grade association consisting of chlorite, epidote, albite, quartz and calcite. Chlorite thermometry indicates T-values in the range of 284 to 352 °C, no variations in mineral composition or T-values were observed among different cataclastic units. Mass balance and volume change calculations show significantly larger chemical mobility in the protocataclasites than in the cataclasite (and ultracataclasite). This suggests that fluid flow and chemical alteration are strongly controlled by deformation being protocataclasite relatively more permeable than cataclasite. Chlorite precipitation and grain reduction in cataclasite (and ultracataclasite) would reduce permeability acting as a barrier for fluid flow. Chemical mobility and volume changes in the Coloso Fault core suggest different effective fluid/flow ratios during amalgamation of subsequent and subparallel deformation bands that finally control the fracture–channeling allowing fault-related fluid–flow into each of them.

1. Introduction

Exhumed faults can be used as natural laboratories, where the interplay among deformation mechanisms, mineral chemistry, mineral reactions, bulk chemical redistributions, and fluid–rock interaction during deformation can be studied (e.g. Steyrer and Sturm, 2002, and references therein). However, the complexity of deformed rocks makes it difficult to assess these interrelationships; particularly, the interplay between chemical mobility and fluid–rock interaction in fault zones is poorly constrained. The aim of this study is to address the chemical mobility and volume changes associated with hydrothermal alteration in the Caleta Coloso Fault, in order to understand the role of fault zones as a channel/barrier for fluid–flow and fluid–rock interactions.

* Corresponding author at: Department of Structural and Geotechnical Engineering, Pontificia Universidad Catolica de Chile, Avenida Vicuña Mackenna 4860, Macul, Santiago, Chile. Tel.: +56 2 23541505.
E-mail addresses: garancibia@ing.puc.cl (G. Arancibia), piyo.102483@gmail.com (K. Fujita), hoshino@hiroshima-u.ac.jp (K. Hoshino), tom.mitchell@ucl.ac.uk (T.M. Mitchell), jcembrano@ing.puc.cl (J. Cembrano), ragomila@uc.cl (R. Gomila), dmorata@ing.uchile.cl (D. Morata), faulkner@liverpool.ac.uk (D.R. Faulkner), marieke.rempe@web.de (M. Rempe).
[1] Now at: Chuden Engineering Consultants Co., Ltd., Japan.
[2] Now at: Department of Earth Sciences, University College London, Gower Street, London WC1E 6BT, United Kingdom.
[3] Now at: Dipartimento di Geoscienze, Università di Padova, Italy.

http://dx.doi.org/10.1016/j.tecto.2014.03.024
0040-1951/

Fault zones have been demonstrated as areas favoring crustal fluid migration. The migration of fluids is important for several reasons. Fluid pressure redistribution can result in the triggering of earthquakes (e.g. Miller et al., 1996) and aftershock sequences (Miller et al., 2004). Additionally, faults might help to maintain hydrostatic pore pressures, which will maintain typical brittle crustal strength. When fluid–rock interaction occurs during fluid migration, bulk mineralogical changes promoted by dissolution/precipitation of minerals involving selective chemical mobility and volume changes can promote significant changes in fault–rock strength (Holdsworth, 2004). The processes are strongly controlled by permeability, porosity and temperature (e.g. Evans and Chester, 1995; Faulkner et al., 2010; O'Hara, 1988; Selverstone et al., 1991, and references therein).

Fluid mobility has been inferred when the geochemical signature and structure of fault core are analyzed in detail, in contrast with the damage zone or undeformed protolith (e.g. Hammond and Evans, 2003). Evans and Chester (1995) show how significant chemical variations are mostly restricted to a discrete zone only several meters wide, whereas to outside this zone, the protolith exhibits significantly lower alteration with minimum chemical mobility. Although various authors have studied fluid–flow properties and the mechanical behavior of fault zones, little quantification about chemical mobility is yet available. However, previous works quantifying chemical mobility and volume changes include Goddard and Evans (1995), Hippertt (1998), Kwon et al., 2009, O'Hara (1988), O'Hara and Blackburn (1989) and Steyrer and Sturm (2002). Most of these studies determine the chemical mobility and volume change using major and trace element signatures in deformed versus undeformed rocks.

Bearing in mind the importance of fault zones for fluid migration on a crustal scale, a detailed analysis of hydrothermal alteration has been made in the regional contact between the damage zone and fault core of Caleta Coloso Fault, a major strike-slip brittle fault in Northern Chile. This fault has a superb exposure and continuous outcrops across and along fault-strike. Petrographic studies are used to characterize different components of the fault zone. The mineral chemistry and whole-rock geochemistry of these fault zone components were conducted, and the physical and chemical conditions of the fluids yielding the hydrothermal alteration are constrained. Caleta Coloso Fault is a crustal scale structure, passively exhumed from 5 to 10 km depth, and exposure in an arid to hyperarid environment, reducing weathering interaction. Low porosity and low altered host rocks are good examples to constrain the relationship between the multiple fault core architecture and fluid–rock interaction and evolution.

2. Geological setting

The Atacama Fault System (AFS) is a ca. 1000 km long trench-parallel large-scale structure that runs between Iquique and La Serena (e.g. Cembrano et al., 2005), and is developed within the Mesozoic rocks of the present-day Coastal Cordillera in Northern Chile. The AFS initiated during Lower Cretaceous times, in part simultaneously with the development of the Jurassic to Lower Cretaceous magmatic arc under a ductile deformational regime, until cooling and tectonic exhumation began at ca. 125 Ma (Scheuber and Gonzalez, 1999), where a brittle deformational regime dominated (e.g. Herrera et al., 2005; Jensen et al., 2011; Olivares et al., 2010). The well-documented left-lateral strike-slip movement has been interpreted as the result of the SE-ward oblique subduction of the Aluk (Phoenix) oceanic plate between 190 and 110 Ma (Grocott et al., 1994; Scheuber and Andriessen, 1990; Scheuber and Gonzalez, 1999). Recent activity of the AFS has been documented mainly as extensional and interpreted as a reactivation of the system in response to mega-thrust earthquakes (e.g. Cortes et al., 2012; Gonzalez et al., 2006; Naranjo, 1987).

The Caleta Coloso Fault (Fig. 1) is an important tectonic structure within the AFS, and is represented as a ca. 80 km long, N–S to NNW–SSE trending strike-slip fault. According to Cembrano et al. (2005),

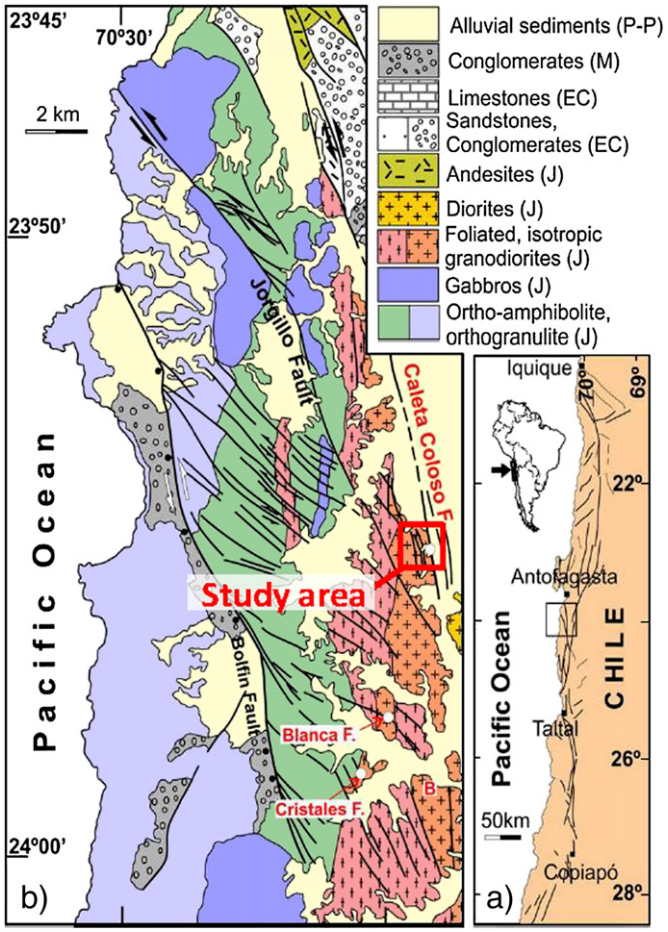

Fig. 1. Regional geological map showing the Caleta Coloso Fault zone and study area (Modified from Cembrano et al., 2005).

this fault shows a left-lateral displacement of about 5 km and a subvertical dip. The fault cuts through Jurassic crystalline rocks of predominantly granodioritic–tonalitic composition (Gonzalez and Niemeyer, 2005) and its fault core currently displays hydrothermally-altered cataclastic rocks with a variable thickness between 200 and 600 m (Faulkner et al., 2008; Olivares et al., 2010). Close to the regional southern end of the fault (red box in Fig. 1), the contact between the damage zone and the cataclastic core zone is very well exposed (Fig. 2). Here, detailed structural mapping showed that the density of fluid inclusion planes, and thus of microfractures, increases toward the fault core (Mitchell and Faulkner, 2009). The fault core is surrounded by a fracture damage zone up to 150 m (Mitchell and Faulkner, 2009). The fault core incorporates multiple strands of variably-deformed fault rock, and is characterized by a green coloration due to the mineralization of chlorite and epidote in both veins and the bulk fault rock. The wide nature of the fault core has previously been interpreted as the result of syn-deformation precipitation healing, leading to spatially and temporally localized strengthening resulting in distributed deformation (Faulkner et al., 2008). The study area (ca. 450×250 m^2) centers on the contact between the damage zone and core of the Caleta Coloso Fault, which has already been the site of several published studies (Faulkner et al., 2006; Faulkner et al., 2008; Mitchell and Faulkner, 2009). The damage zone (150 m of effective damage zone wide, Faulkner et al., 2010) shows a rather homogeneous and weakly altered tonalitic host rock with a network of crossing centimeter-wide calcite–quartz–epidote veins. The fault core (up to 500 m wide, Cembrano et al.,

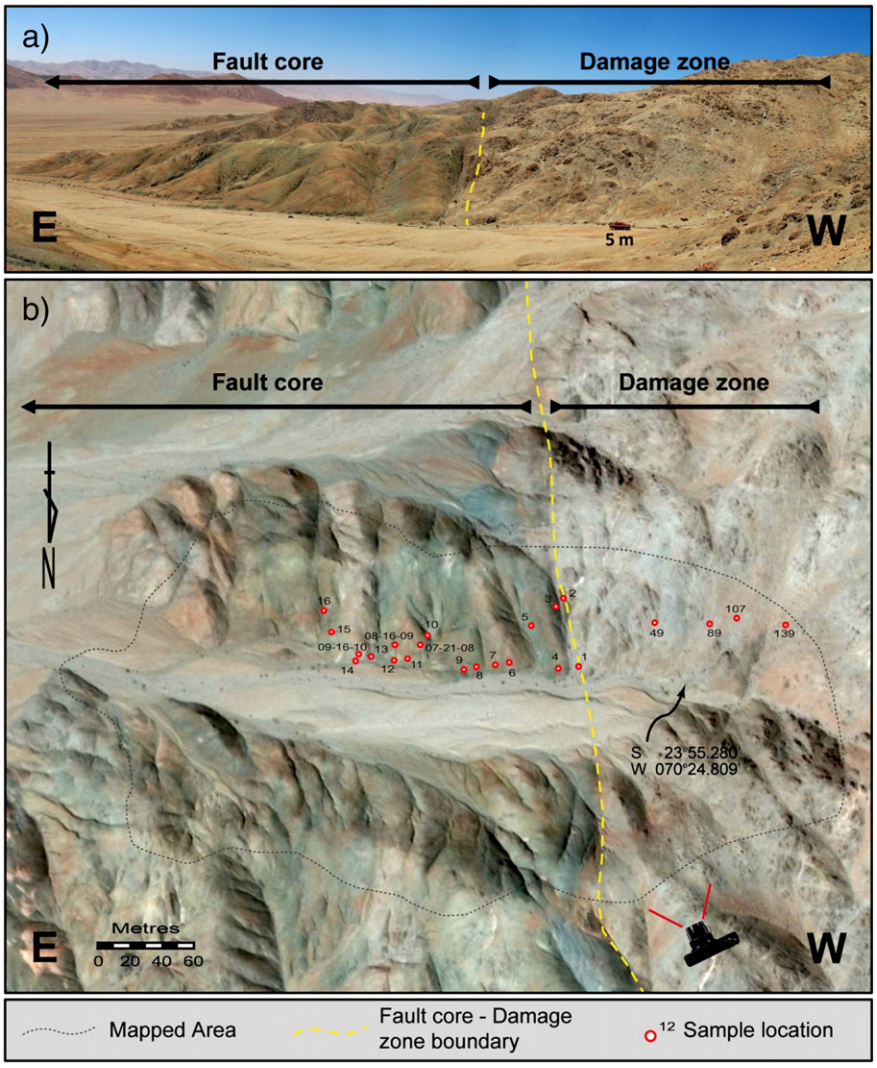

Fig. 2. (a) Panoramic view of the Caleta Coloso Fault zone looking to the south. Yellow dotted line defines the damage zone to the west and the core zone to the east. (b) Satellite image from the Caleta Coloso Fault zone, showing regional damage zone and fault core.

2005) consists of subparallel NS-striking bands of varying low to high strain rocks: undeformed protolith, weakly deformed protolith, protocataclasite, cataclasite and ultracataclasite (Fig. 3 and Table 1).

3. Sampling and analytical methods

Hand specimens, 0.5 to 1 kg, were taken across a total ca. 400 m profile orthogonal to the fault zone strike, including damage and core zones. Samples were selected with the aim to cover all fault rock lithologies previously described and observed in the profile (Fig. 3). Representative samples from damage zone were selected avoiding undesired contamination by crossing veins and/or intense fracture density, showing rather homogeneous texture at least at the outcrop scale. For the core fault zone, samples were taken avoiding, when possible, crossing veinlets. When feasible, at least one representative sample was taken for each subparallel NS-striking band. The cleanest small chips were selected in the field and finally prepared in laboratory for chemical analyses (WC mortar milling) and petrographic thin sections.

A total of twenty three samples were taken in the cross section for geochemical and microstructural analyses along a 300 m sampling transect (Fig. 2): 4 samples from the damage zone (samples 49, 89, 107 and 139) and 19 samples from the fault core zone (samples 01 to 16 and samples 091610, 081609, 072108). Label of samples from damage zone represents distance (in meters) from the fault core/damage zone contact (Fig. 3). These samples are considered as representative of host rock whereas sample 139 m represents the limit of effective damage zone, with microfracture density equivalent to that of the background (Faulkner et al., 2010).

Samples from fault core consist of 3 rocks from relict protolith bands into fault core, 6 from weakly deformed protolith, 5 from protocataclasite bands and 4 samples from cataclasite bands. Only one sample from ultracataclasite band was sampled, because it is the unique band available to mapping scale (ca. 1 m width). The mineral chemistry of plagioclase, hornblende, epidote and chlorite was obtained by wavelength-dispersive electron microprobe analyses (EMPAs), which were carried out in polished thin sections using a JEOL-JXA-8200 at Hiroshima University, Japan. Analytical conditions were 15 kV as accelerating voltage, a beam current of 12 nA and a spot size of 5 to 2 μm. Wollastonite (Si and Ca), rutile (Ti), corundum (Al), hematite (Fe), manganosite (Mn), eskolaite (Cg), periclase (Mg), albite (Na) and adularia (K) were used as standards. EMPAs of minerals are presented in Tables 2, 3 and 4.

Bulk chemistry of samples was determined by X-ray fluorescence spectrometry (XRF) using a Philips PW 2400 at the Faculty of Geosciences, Ruhr Universität, Bochum, Germany. After crushing and milling, ca. 1 g of

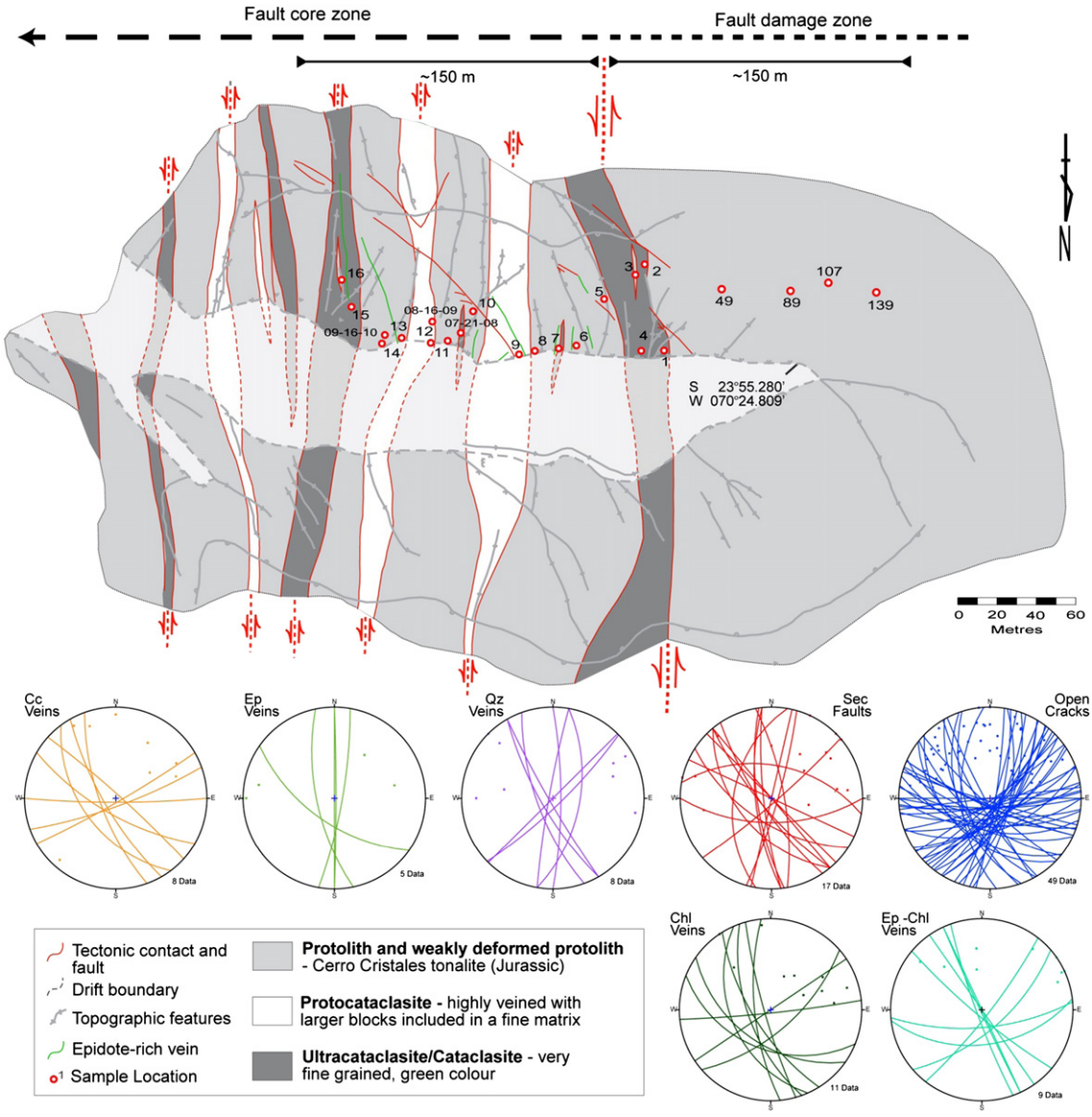

Fig. 3. Simplified geological map of the fault core (modified from Faulkner et al., 2008) and sample location. Stereoplots show orientations of veins, secondary faults and open cracks.

powdered samples was fused with Spectromelt® to prepare glass disk for the analyses of major elements. Trace elements were determined using a powder pellet. Internal standards of granite, orthoclase and diorite were used during major element determinations and granite and basalt for trace element analyses. Major (expressed as weight percent oxides) and selected trace (quoted in ppm) elements together with measured densities (ρ) are quoted in Table 5.

4. Results

4.1. Petrography and microstructure

Based on mesoscopic and microscopic textural observations, samples from the fault core zone were classified into 1) protolith, 2) weakly deformed protolith, 3) protocataclasite, 4) cataclasite and 5) ultracataclasite

Table 1
Textural classification for rocks from Caleta Coloso Fault core, Atacama Fault Zone, Chile.

Sample	Texture	Alteration	Rock type
1, 11, 6	Undeformed tonalite. Preserved primary texture.	Amphibole and biotite partially replaced by chlorite. Incipient albitization.	Protolith
10, 13, 8, 14, 5, 09_16_10	Undeformed tonalite. Preserved primary texture. Partially crossed by calcite–quartz–epidote–chlorite veins.	Amphibole and biotite partially replaced by chlorite. Incipient albitization.	Weakly deformed protolith
9, 12, 16, 3, 08_16_09	Preserved primary texture. Strongly crossed by calcite–quartz–epidote–chlorite veins. Coarse grain size.	Chlorite–epidote–albite–quartz–calcite. Epidote > chlorite.	Protocataclasite
15, 4, 7, 07_21_08	Cataclastic foliated texture. Fine grain size.	Chlorite–epidote–albite–quartz–calcite. Chlorite > epidote.	Cataclasite
2	Very fine grained cataclastic/mylonitic foliated texture.	Pervasive alteration. Clay minerals.	Ultracataclasite

(Table 1, Figs. 4 and 5). The protolith corresponds to undeformed to slightly deformed metric elongated lenses of hypidiomorphic porphyritic hornblende tonalite with grain sizes ranging from ca. 0.5 to 4 mm, which is similar to the low altered host rock of the Caleta Coloso Fault sampled in the damage zone (samples 49, 89, 107 and 139, Fig. 3). The tonalite protolith is only weakly altered and its major mineralogical components are ca. 55% plagioclase, 28% quartz, 10% hornblende, 8% biotite, trace to <2% clinopyroxene and 2% magnetite. Biotite and hornblende show poikilitic texture and both are locally replaced by chlorite and minor amounts of epidote. Plagioclase crystals show a weak N–S to NE preferred magmatic orientation, as shown by polysynthetic twinning. Small amounts of sericite fill plagioclase fractures. Anhedral quartz crystals exhibit undulose extinction (Fig. 5a). In the damage zone, samples selected as representative of the host rock only show light felsic/mafic mineral variations, in concordance with the rather homogeneous chemical composition (see Section 4.3).

The weakly deformed protolith, with a relative higher degree of alteration, consists of tonalite that is cross-cut by epidote–chlorite veins. Plagioclase crystals are completely replaced by sericite, such are hornblende and biotite by chlorite, with pseudomorphous replacement textures in the biotite. The primary hydrothermal minerals are epidote, chlorite, albite and calcite, with chlorite being more abundant than epidote. Quartz crystals show undulose extinction and form polycrystalline quartz aggregates with irregular grain boundaries (Fig. 5b).

Protocataclasites are developed from the tonalite protolith, but are heavily cross-cut by quartz, epidote and chlorite veins and thin anastomosing cataclastic bands with a small degree of grain comminution, and up to 15% of matrix content, hosting protolith fragments that preserve the primary igneous texture. The degree of alteration observed in the protocataclasites is similar to that observed in the weakly deformed protolith. The primary hydrothermal minerals are epidote, chlorite, quartz, albite and calcite, again with epidote generally more abundant than chlorite. Quartz crystals show undulose extinction, and better developed polycrystalline quartz aggregates with irregular grain boundaries (Fig. 5c).

Cataclasites show a foliated matrix and cataclastic texture, significantly reduced grain size (ca. 0.5 to 5 mm) and a matrix content as high as 70%. The grains vary from pods of protolith to single quartz and plagioclase crystal fragments. Alteration is similar to that of the protocataclastic rocks, but with chlorite occurring as the dominant mineral. Thin quartz and calcite veins (ca. 0.01 mm thick) with minor Fe-oxides can be also observed (Fig. 5d).

The ultracataclasite shows a fine-grained and strongly-foliated cataclastic/mylonitic texture, where the ductile deformation of quartz is overprinted by the brittle deformation features. The matrix content is >90%, and the visible fragments are primarily quartz (ca. 55% to 70%), plagioclase (ca. 30% to 40%) and clasts of cataclasite (ca. 5% to 15%). Alteration mineralogy is similar to that of the other fault rocks, dominated by clay minerals, but the extreme grain size reduction hinders the exact mineral identification in the comminuted bands (Fig. 5e).

4.2. Mineral chemistry

EMPA results indicate that primary plagioclase ranges in composition from $An_{53}Ab_{47}Or_0$ to $An_{36}Ab_{63}Or_1$, with slight albitization ($An_{13}Ab_{86}Or_1$) along the rims within the protolith (Table 2). Stronger albitization ($An_7Ab_{93}Or_0$) is observed in the cataclastic rocks, showing relics of anorthitic patches in several plagioclase crystals. The highest albitic content ($An_1Ab_{99}Or_0$) is observed in the ultracataclasite, but even in these strongly altered rocks small patches of anorthitic relics ($An_{57-31}Ab_{43-69}Or_0$) remain in the core of some crystals. Amphibole does not show a significant compositional variation between the protolith and deformed rocks. Their chemical composition indicates that the amphiboles can be classified as hornblende, with Mg/(Mg + Fe) ranging from 0.64 to 0.60 and Al_{tot} from 1.446 to 1.304 a.p.f.u. (Table 3).

Along with partial to total albitization, epidote and chlorite are the principal alteration minerals. Epidote is present in all 5 rock types, having higher proportions in the protocataclasite. No major differences have been identified in epidote chemistry among different rock types, obtaining a similar chemical range in all samples (Table 3). The epidote from the protolith exhibits the highest Fe values relative to Al ($Fe^{3+}/(Fe^{3+} + Al) = 0.21–0.32$).

Chlorite also shows a relatively homogeneous chemical composition in all different rock types (Table 4). The most significant chemical variation observed is in the Mg/Fe ratio ($Mg/(Mg + Fe^{2+}) = 0.64$ to 0.53. Si ranges from 5.429 to 5.855 a.p.f.u. and the sum of interlayered cations (IC = Ca + Na + K) ranges from 0.066 to 0.000 a.p.f.u., with a total of octahedral cations ranging from 11.755 to 11.989 a.p.f.u. These chemical characteristics are indicative of almost pure chlorite with minimum smectite content, and a relatively homogeneous compositional range. Moreover, the ratio of smectite to chlorite (X_c in Table 4) estimated by the Wise's method based on chemical data for Ca, Na and K obtained from EMPA (Bettison and Schiffman, 1988; Bettison-Varga et al., 1991; Bevins et al., 1991) ranges from 0.845 to 0.973, supporting the high chlorite component of these mafic phyllosilicates. Miyahara et al. (2005) demonstrated that when the IC is <0.10 per chlorite unit, these cations are present in the smectite layers and not as discrete phases (impurities) such as calcite and albite in the chlorite aggregate.

Mineral associations were plotted in ACF diagrams (Fig. 6), as are the chemical changes in both whole rock and minerals during alteration. In all cases, mineral compositions are consistent with the whole-rock chemistry, where the main chemical variations observed in primary and neoformed minerals are also represented. In the protolith, the mineral assemblage changes from plagioclase + hornblende + biotite (the F corner in the diagram), to plagioclase + chlorite + epidote in the cataclastic rocks. The ratios of the protocataclastic rocks shift toward the C corner resulting in the formation of the assemblage chlorite + epidote + calcite, showing a remarkable similarity in the projections for both protolith and ultracataclastic fault rocks.

4.3. Geochemistry

Major and selected trace elements for whole-rock XRF analyses and measured densities are quoted in Table 5. The four selected samples for tonalite host rock cover the different petrographic variations observed across the ca. 150 m of damage zone. Geochemical data suggests a rather homogeneous composition with low standard deviation (Fig. 7 and Table 5) allowing us to consider the average value as baseline for quantifying gain and loss of elements of the core fault samples. As deduced from petrography, only small variations in TiO_2, Fe_2O_3, MgO and CaO are observed in relation with the variable distribution of light and dark minerals.

Concerning the defined textural classification for rocks from the fault core zone (Table 1), geochemical data were also plotted in Fig. 7 with the aim to check if measured values fall into the primary geochemical variation (baseline, Fig. 7a) or spread these values.

The metric elongated lenses of protolith show a similar geochemical pattern than that of the baseline (Fig. 7b) and only a slight decrease in CaO coupled with a slight increase in NaO_2 (associated with the albitization of primary plagioclase) is observed. A LOI increase (up to 3.70 wt.%) is also evident and is consistent with the increase of clay minerals and calcite in the hydrothermal alteration related with faulting. As expected, the weakly deformed protolith shows a similar pattern (Fig. 7c). On the contrary, the highest dispersion of most major elements is observed in protocataclasite (Fig. 7d). Increasing in SiO_2, Na_2O and LOI and decreasing in TiO_2, Fe_2O_3, CaO, MgO, MnO and K_2O are related to the highest alteration degree observed to be associated with pervasive albitization, epidote abundance, chloritization of primary mafic minerals and magnetite oxidation. Also, the presence of microveinlets (filled by alteration minerals) would favor the geochemical heterogeneity observed in these rocks. The high variation range

Table 2
EMPA data and structural formula of plagioclase (Pl) based on 8 oxygens from rocks of Coloso Fault core: protolith (Proto), weakly deformed protolith (WDefP), protocataclasite (Pcata), cataclasite (Cata) and ultracataclasite (Ucata). Percentage of anorthite (An), albite (Ab) and orthoclase (Or) is given.

Sample	1	1	1	1	1	1	11	11	6	6	6	5	5	5	5	5	10	10	10	10	13
Texture	Proto	Proto	Proto	Proto	Proto	Proto	Proto	Proto	Proto	Proto	Proto	WDefP	WDefP	WDefP	WDefP	WDefP	WDefP	WDefP	WDefP	WDefP	WDefP
Mineral	Pl	Pl	Pl	Pl	Pl	Pl	Pl	Pl	Pl	Pl	Pl	Pl	Pl	Pl	Pl	Pl	Pl	Pl	Pl	Pl	Pl
SiO_2	57.27	55.76	55.84	57.74	54.56	56.98	56.98	57.10	57.59	56.90	58.91	58.81	57.34	57.61	58.34	56.79	63.97	60.46	59.99	64.69	58.64
TiO_2	0.00	0.00	0.00	0.00	0.00	0.00	0.00	0.03	0.01	0.00	0.00	0.01	0.00	0.00	0.05	0.01	0.00	0.00	0.00	0.00	0.05
Al_2O_3	26.12	27.38	27.17	25.91	28.36	26.74	26.69	26.59	26.45	26.88	25.55	25.94	26.34	25.80	25.63	26.91	22.18	24.23	24.95	21.54	25.62
Cr_2O_3	0.00	0.02	0.04	0.00	0.00	0.01	0.00	0.01	0.03	0.03	0.00	0.00	0.00	0.01	0.01	0.01	0.02	0.00	0.00	0.01	0.02
FeO	0.09	0.09	0.10	0.08	0.06	0.12	0.06	0.06	0.09	0.11	0.11	0.04	0.00	0.06	0.12	0.11	0.05	0.14	0.08	0.05	0.13
MnO	0.05	0.00	0.03	0.01	0.06	0.00	0.02	0.00	0.01	0.06	0.02	0.02	0.02	0.01	0.01	0.00	0.00	0.01	0.00	0.00	0.01
MgO	0.00	0.00	0.00	0.00	0.01	0.00	0.00	0.00	0.01	0.01	0.01	0.01	0.00	0.00	0.00	0.01	0.01	0.01	0.00	0.00	0.00
CaO	8.53	9.34	9.74	7.79	10.90	8.95	8.73	8.94	8.47	8.82	7.57	7.77	8.44	8.22	7.62	8.76	3.39	6.27	6.53	2.77	7.66
Na_2O	6.52	5.85	6.10	7.03	5.39	6.52	6.37	6.59	6.64	6.48	7.05	7.27	6.85	6.94	7.32	6.46	9.68	7.95	7.85	9.92	7.34
K_2O	0.05	0.04	0.07	0.08	0.07	0.11	0.12	0.13	0.10	0.09	0.09	0.07	0.08	0.11	0.09	0.06	0.10	0.20	0.15	0.12	0.09
Total	98.63	98.48	99.09	98.64	99.41	99.43	98.97	99.45	99.40	99.38	99.31	99.94	99.07	98.76	99.19	99.12	99.40	99.27	99.55	99.10	99.56
Si	2.598	2.538	2.534	2.616	2.475	2.571	2.578	2.575	2.593	2.567	2.646	2.629	2.592	2.611	2.629	2.567	2.838	2.710	2.683	2.872	2.633
Ti	0.000	0.000	0.000	0.000	0.000	0.000	0.000	0.001	0.000	0.000	0.000	0.000	0.000	0.000	0.002	0.000	0.000	0.000	0.000	0.000	0.002
Al	1.397	1.469	1.453	1.384	1.517	1.422	1.423	1.414	1.404	1.429	1.352	1.367	1.403	1.378	1.361	1.434	1.160	1.280	1.315	1.127	1.356
Cr	0.000	0.001	0.001	0.000	0.000	0.000	0.000	0.000	0.001	0.001	0.000	0.000	0.000	0.000	0.000	0.000	0.001	0.000	0.000	0.000	0.001
Fe^{2+}	0.003	0.003	0.004	0.003	0.002	0.005	0.002	0.002	0.003	0.004	0.004	0.001	0.000	0.002	0.005	0.004	0.002	0.005	0.003	0.002	0.005
Mn^{2+}	0.002	0.000	0.001	0.000	0.002	0.000	0.001	0.000	0.000	0.002	0.001	0.001	0.001	0.000	0.000	0.000	0.000	0.000	0.000	0.000	0.000
Mg	0.000	0.000	0.000	0.000	0.001	0.000	0.000	0.000	0.001	0.001	0.001	0.001	0.000	0.000	0.000	0.001	0.001	0.001	0.000	0.000	0.000
Ca	0.415	0.456	0.474	0.378	0.530	0.433	0.423	0.432	0.409	0.426	0.364	0.372	0.409	0.399	0.368	0.424	0.161	0.301	0.313	0.132	0.369
Na	0.574	0.516	0.537	0.618	0.474	0.570	0.559	0.576	0.580	0.567	0.614	0.630	0.600	0.610	0.640	0.566	0.833	0.691	0.681	0.854	0.639
K	0.003	0.002	0.004	0.005	0.004	0.006	0.007	0.007	0.006	0.005	0.005	0.004	0.005	0.006	0.005	0.003	0.006	0.011	0.009	0.007	0.005
Ba	0.000	0.000	0.000	0.000	0.000	0.000	0.000	0.000	0.000	0.000	0.000	0.000	0.000	0.000	0.000	0.000	0.000	0.000	0.000	0.000	0.000
Σcations	4.991	4.986	5.009	5.003	5.005	5.007	4.993	5.008	4.997	5.003	4.987	5.005	5.009	5.008	5.010	5.000	5.001	5.001	5.004	4.994	5.009
%An	41.84	46.76	46.69	37.80	52.56	42.86	42.79	42.53	41.11	42.70	37.04	36.98	40.32	39.31	36.33	42.69	16.12	30.01	31.22	13.28	36.39
%Ab	57.87	53.00	52.91	61.73	47.04	56.51	56.51	56.73	58.32	56.78	62.43	62.62	59.22	60.06	63.16	56.97	83.31	68.85	67.92	86.04	63.10
%Or	0.29	0.24	0.40	0.46	0.40	0.63	0.70	0.74	0.58	0.52	0.52	0.40	0.46	0.63	0.51	0.35	0.57	1.14	0.85	0.68	0.51

Table 2 (*continued*)

Sample	13	13	14	14	9	9	9	9	9	12	12	16	3	3	15	4	4	4	2	2	2	2
Texture	WDefP	WDefP	WDefP	WDefP	Pcata	Pcata	Pcata	Pcata	Pcata	Pcata	Pcata	Pcata	Pcata	Pcata	Cata	Cata	Cata	Cata	Ucata	Ucata	Ucata	Ucata
Mineral	Pl	Pl	Pl	Pl	Pl	Pl	Pl	Pl	Pl	Pl	Pl	Pl	Pl	Pl	Pl	Pl	Pl	Pl	Pl	Pl	Pl	Pl
SiO_2	57.01	58.53	59.48	57.38	67.11	67.47	66.51	67.19	66.66	66.89	67.50	66.43	66.91	67.33	64.54	55.99	54.61	59.94	53.03	59.58	68.08	57.77
TiO_2	0.05	0.00	0.00	0.02	0.00	0.00	0.04	0.04	0.00	0.00	0.00	0.00	0.01	0.01	0.02	0.03	0.00	0.00	0.05	0.00	0.03	0.02
Al_2O_3	26.49	25.59	24.73	25.97	20.35	20.16	20.34	20.30	20.25	20.26	19.84	20.80	19.90	19.66	21.61	27.16	27.61	24.35	29.21	24.91	19.59	26.61
Cr_2O_3	0.01	0.00	0.00	0.03	0.00	0.00	0.01	0.02	0.00	0.00	0.00	0.00	0.00	0.00	0.00	0.00	0.00	0.04	0.01	0.00	0.00	0.01
FeO	0.09	0.08	0.08	0.06	0.02	0.00	0.09	0.05	0.02	0.01	0.01	0.01	0.01	0.02	0.14	0.08	0.09	0.17	0.17	0.11	0.07	0.02
MnO	0.00	0.00	0.00	0.00	0.00	0.00	0.00	0.01	0.00	0.03	0.01	0.01	0.02	0.00	0.00	0.00	0.03	0.04	0.01	0.00	0.00	0.00
MgO	0.01	0.00	0.00	0.01	0.00	0.01	0.04	0.00	0.02	0.00	0.00	0.00	0.00	0.00	0.00	0.01	0.00	0.01	0.01	0.00	0.00	0.00
CaO	8.68	7.65	6.64	8.14	1.04	0.84	1.16	0.84	0.98	1.08	0.73	1.57	0.91	0.37	2.46	9.54	10.09	6.18	11.48	6.63	0.25	8.63
Na_2O	6.76	7.30	7.76	7.00	11.14	11.19	10.94	11.21	10.99	11.30	11.42	11.08	11.31	11.83	10.14	6.26	6.13	8.20	4.79	7.98	11.69	6.89
K_2O	0.13	0.15	0.11	0.06	0.10	0.07	0.08	0.08	0.09	0.09	0.08	0.05	0.07	0.06	0.07	0.08	0.11	0.13	0.05	0.06	0.06	0.06
Total	99.23	99.30	98.80	98.67	99.76	99.74	99.21	99.74	99.01	99.66	99.59	99.95	99.14	99.28	98.98	99.15	98.67	99.06	98.81	99.27	99.77	100.01
Si	2.577	2.634	2.681	2.603	2.947	2.959	2.938	2.950	2.947	2.943	2.967	2.918	2.957	2.970	2.869	2.538	2.497	2.697	2.425	2.675	2.984	2.588
Ti	0.002	0.000	0.000	0.001	0.000	0.000	0.001	0.001	0.000	0.000	0.000	0.000	0.000	0.000	0.001	0.001	0.000	0.000	0.002	0.000	0.001	0.001
Al	1.411	1.358	1.314	1.389	1.053	1.042	1.059	1.050	1.055	1.051	1.028	1.077	1.036	1.022	1.132	1.451	1.488	1.291	1.574	1.318	1.012	1.405
Cr	0.000	0.000	0.000	0.001	0.000	0.000	0.000	0.001	0.000	0.000	0.000	0.000	0.000	0.000	0.000	0.000	0.000	0.001	0.000	0.000	0.000	0.000
Fe^{2+}	0.003	0.003	0.003	0.002	0.001	0.000	0.003	0.002	0.001	0.000	0.000	0.000	0.000	0.001	0.005	0.003	0.003	0.006	0.007	0.004	0.003	0.001
Mn^{2+}	0.000	0.000	0.000	0.000	0.000	0.000	0.000	0.000	0.000	0.001	0.000	0.000	0.001	0.000	0.000	0.000	0.001	0.002	0.000	0.000	0.000	0.000
Mg	0.001	0.000	0.000	0.001	0.000	0.001	0.003	0.000	0.001	0.000	0.000	0.000	0.000	0.000	0.000	0.001	0.000	0.001	0.001	0.000	0.000	0.000
Ca	0.420	0.369	0.321	0.396	0.049	0.039	0.055	0.040	0.046	0.051	0.034	0.074	0.043	0.017	0.117	0.463	0.494	0.298	0.563	0.319	0.012	0.414
Na	0.593	0.637	0.678	0.616	0.948	0.952	0.937	0.954	0.942	0.964	0.973	0.944	0.969	1.012	0.874	0.550	0.543	0.715	0.425	0.695	0.993	0.598
K	0.007	0.009	0.006	0.003	0.006	0.004	0.005	0.004	0.005	0.005	0.004	0.003	0.004	0.003	0.004	0.005	0.006	0.007	0.003	0.003	0.003	0.003
Ba	0.000	0.000	0.000	0.000	0.000	0.000	0.000	0.000	0.000	0.000	0.000	0.000	0.000	0.000	0.000	0.000	0.000	0.000	0.000	0.000	0.000	0.000
Σcations	5.015	5.010	5.004	5.011	5.004	4.997	5.001	5.003	4.998	5.016	5.008	5.016	5.011	5.026	5.003	5.012	5.034	5.018	4.999	5.015	5.008	5.010
%An	41.20	36.36	31.90	38.99	4.88	3.97	5.51	3.96	4.67	4.99	3.40	7.24	4.24	1.69	11.77	45.51	47.34	29.19	56.81	31.36	1.16	40.77
%Ab	58.06	62.79	67.47	60.67	94.56	95.64	94.04	95.59	94.82	94.51	96.16	92.48	95.37	97.98	87.83	54.04	52.05	70.08	42.90	68.30	98.50	58.90
%Or	0.73	0.85	0.63	0.34	0.56	0.39	0.45	0.45	0.51	0.50	0.44	0.27	0.39	0.33	0.40	0.45	0.61	0.73	0.29	0.34	0.33	0.34

Table 3
EMPA data and structural formula of amphibole (Amph) and epidote (Ep) based on 23 and 12.5 oxygens respectively, from rocks of Caleta Coloso Fault core: protolith (Proto), weakly deformed protolith (WDefP), protocataclasite (Pcata), cataclasite (Cata) and ultracataclasite (Ucata).

Sample	1	11	6	14	7	1	1	11	11	6	6	5	5	10	10	13
Texture	Proto	Proto	Proto	Proto	Cata	Proto	Proto	Proto	Proto	Proto	Proto	Proto	Proto	WDefP	WDefP	WDefP
Mineral	Amph	Amph	Amph	Amph	Amph	Ep	Ep	Ep	Ep	Ep	Ep	Ep	Ep	Ep	Ep	Ep
SiO_2	46.26	47.25	45.91	46.08	47.00	37.54	36.94	37.22	37.68	37.46	37.88	37.82	38.14	37.50	37.85	37.62
TiO_2	1.69	1.62	1.21	1.14	1.76	0.06	0.02	0.53	0.16	0.24	0.15	0.38	0.11	0.58	0.19	0.14
Al_2O_3	8.26	7.50	7.92	7.92	8.03	23.11	21.41	20.90	24.08	22.28	24.40	21.62	24.79	21.99	24.73	23.50
Cr_2O_3	0.00	0.04	0.00	0.02	0.00	0.01	0.00	0.00	0.00	0.00	0.01	0.00	0.03	0.04	0.00	0.01
FeO	13.64	12.54	14.75	14.85	13.78	11.67	14.26	13.73	10.48	12.38	10.22	12.45	10.28	12.43	10.18	11.40
MnO	0.77	0.77	1.00	0.79	0.76	0.40	0.18	0.32	0.33	0.37	0.45	0.16	0.36	0.14	0.26	0.37
MgO	13.29	14.29	12.77	12.56	13.43	0.02	0.00	0.03	0.10	0.05	0.12	0.05	0.04	0.07	0.03	0.04
CaO	11.12	11.03	11.08	11.67	11.08	22.96	22.98	22.71	22.99	22.41	23.03	23.21	23.71	22.92	23.50	22.91
Na_2O	1.13	1.18	1.15	1.00	0.88	0.00	0.01	0.00	0.00	0.00	0.00	0.00	0.00	0.01	0.00	0.00
K_2O	0.42	0.32	0.34	0.28	0.36	0.00	0.01	0.02	0.09	0.00	0.01	0.02	0.00	0.00	0.00	0.01
Total	96.58	96.54	96.13	96.31	97.08	95.77	95.81	95.46	95.91	95.19	96.27	95.71	97.46	95.68	96.74	96.00
Si	6.873	6.973	6.899	6.911	6.930	3.016	2.991	3.021	3.012	3.030	3.013	3.048	3.000	3.022	2.997	3.011
Al^{IV}	1.127	1.027	1.101	1.089	1.070	0.000	0.009	0.000	0.000	0.000	0.000	0.000	0.000	0.000	0.003	0.000
Ti	0.189	0.180	0.137	0.129	0.195	0.004	0.001	0.032	0.010	0.015	0.009	0.023	0.007	0.035	0.011	0.008
Al^{VI}	0.319	0.277	0.301	0.311	0.326	2.188	2.034	1.999	2.268	2.124	2.287	2.054	2.298	2.088	2.304	2.217
Cr	0.000	0.005	0.000	0.002	0.000	0.782	0.963	0.929	0.698	0.835	0.678	0.837	0.674	0.835	0.672	0.761
Fe^{2+}	1.695	1.548	1.854	1.862	1.699	0.001	0.000	0.000	0.000	0.000	0.001	0.000	0.002	0.003	0.000	0.001
Mn^{2+}	0.097	0.096	0.127	0.100	0.095	0.027	0.012	0.022	0.022	0.025	0.030	0.011	0.024	0.010	0.017	0.025
Mg	2.943	3.144	2.861	2.808	2.952	0.002	0.000	0.004	0.012	0.006	0.014	0.006	0.005	0.008	0.004	0.005
Ca	1.770	1.744	1.784	1.875	1.750	1.976	1.994	1.975	1.969	1.942	1.963	2.004	1.998	1.979	1.993	1.964
Na	0.325	0.338	0.335	0.291	0.252	0.000	0.002	0.000	0.000	0.000	0.000	0.000	0.000	0.002	0.000	0.000
K	0.080	0.060	0.065	0.054	0.068	0.000	0.001	0.002	0.009	0.000	0.001	0.002	0.000	0.000	0.000	0.001
Σcations	15.418	15.392	15.463	15.432	15.337	7.995	8.006	7.984	8.000	7.976	7.996	7.985	8.007	7.981	8.002	7.992

Table 3 (*continued*)

Sample	13	8	8	14	14	9	9	12	12	16	3	15	15	7	7	2	2
Texture	WDefP	WDefP	WDefP	WDefP	WDefP	Pcata	Pcata	Pcata	Pcata	Pcata	Pcata	Cata	Cata	Cata	Cata	Ucata	Ucata
Mineral	Ep	Ep	Ep	Ep	Ep	Ep	Ep	Ep	Ep	Ep	Ep	Ep	Ep	Ep	Ep	Ep	Ep
SiO_2	37.42	37.15	37.83	37.37	37.50	37.85	37.62	37.42	37.15	37.83	37.37	37.30	37.47	37.39	37.97	37.50	37.30
TiO_2	0.16	0.06	0.06	0.08	0.11	0.19	0.14	0.16	0.06	0.06	0.08	0.02	0.02	0.41	0.20	0.11	0.02
Al_2O_3	22.14	22.42	24.17	23.36	24.30	24.73	23.50	22.14	22.42	24.17	23.36	23.51	22.43	22.39	25.18	24.30	23.51
Cr_2O_3	0.01	0.00	0.02	0.02	0.00	0.00	0.01	0.01	0.00	0.02	0.02	0.01	0.07	0.01	0.02	0.00	0.01
FeO	12.84	12.80	10.51	10.95	10.12	10.18	11.40	12.84	12.80	10.51	10.95	11.64	12.12	12.49	9.47	10.12	11.64
MnO	0.38	0.34	0.24	0.17	0.24	0.26	0.37	0.38	0.34	0.24	0.17	0.43	0.79	0.09	0.22	0.24	0.43
MgO	0.01	0.00	0.01	0.00	0.05	0.03	0.04	0.01	0.00	0.01	0.00	0.02	0.02	0.04	0.01	0.05	0.02
CaO	22.81	23.00	23.22	23.29	23.53	23.50	22.91	22.81	23.00	23.22	23.29	22.97	22.61	23.65	23.26	23.53	22.97
Na_2O	0.01	0.00	0.03	0.01	0.01	0.00	0.00	0.01	0.00	0.03	0.01	0.00	0.01	0.04	0.00	0.01	0.00
K_2O	0.00	0.00	0.01	0.00	0.00	0.00	0.01	0.00	0.00	0.01	0.00	0.00	0.02	0.03	0.01	0.00	0.00
Total	95.78	95.77	96.10	95.25	95.86	96.74	96.00	95.78	95.77	96.10	95.25	95.90	95.56	96.54	96.34	95.86	95.90
Si	3.016	2.997	3.016	3.014	2.999	2.997	3.011	3.016	2.997	3.016	3.014	2.993	3.025	2.993	3.009	2.999	2.993
Al^{IV}	0.000	0.003	0.000	0.000	0.001	0.003	0.000	0.000	0.003	0.000	0.000	0.007	0.000	0.007	0.000	0.001	0.007
Ti	0.010	0.004	0.004	0.005	0.007	0.011	0.008	0.010	0.004	0.004	0.005	0.001	0.001	0.025	0.012	0.007	0.001
Al^{VI}	2.103	2.128	2.271	2.221	2.290	2.304	2.217	2.103	2.128	2.271	2.221	2.217	2.135	2.106	2.352	2.290	2.217
Cr	0.863	0.861	0.699	0.736	0.675	0.672	0.761	0.863	0.861	0.699	0.736	0.779	0.816	0.834	0.626	0.675	0.779
Fe^{2+}	0.001	0.000	0.001	0.001	0.000	0.000	0.001	0.001	0.000	0.001	0.001	0.001	0.004	0.001	0.001	0.000	0.001
Mn^{2+}	0.026	0.023	0.016	0.012	0.016	0.017	0.025	0.026	0.023	0.016	0.012	0.029	0.054	0.006	0.015	0.016	0.029
Mg	0.001	0.000	0.001	0.000	0.006	0.004	0.005	0.001	0.000	0.001	0.000	0.002	0.002	0.005	0.001	0.006	0.002
Ca	1.970	1.988	1.984	2.013	2.016	1.993	1.964	1.970	1.988	1.984	2.013	1.975	1.956	2.029	1.975	2.016	1.975
Na	0.002	0.000	0.005	0.002	0.002	0.000	0.000	0.002	0.000	0.005	0.002	0.000	0.002	0.006	0.000	0.002	0.000
K	0.000	0.000	0.001	0.000	0.000	0.000	0.001	0.000	0.000	0.001	0.000	0.000	0.002	0.003	0.001	0.000	0.000
Σcations	7.991	8.004	7.997	8.003	8.012	8.002	7.992	7.991	8.004	7.997	8.003	8.004	7.998	8.013	7.991	8.012	8.004

Table 4
EMPA data and structural formula of chlorite (Chl) based on 28 oxygens from rocks of Caleta Coloso Fault core: protolith (Proto), weakly deformed protolith (WDefP), protocataclasite (Pcata), cataclasite (Cata) and ultracataclasite (Ucata).

Sample	1	1	1	1	1	1	11	11	11	11	6	6	6	6	6	6	5	5	5	5	5	5	5	5
Texture	Proto	Proto	Proto	Proto	Proto	Proto	Proto	Proto	Proto	Proto	Proto	Proto	Proto	Proto	Proto	Proto	WDefP	WDefP	WDefP	WDefP	WDefP	WDefP	WDefP	WDefP
Mineral	Chl	Chl	Chl	Chl	Chl	Chl	Chl	Chl	Chl	Chl	Chl	Chl	Chl	Chl	Chl	Chl	Chl	Chl	Chl	Chl	Chl	Chl	Chl	Chl
SiO_2	26.18	26.23	26.11	26.89	26.42	26.14	26.95	26.47	27.13	27.01	26.51	26.81	26.98	26.71	26.14	26.50	26.82	26.53	26.49	27.10	26.47	26.66	26.47	26.60
TiO_2	0.08	0.03	0.01	0.00	0.07	0.04	0.03	0.04	0.08	0.05	0.05	0.00	0.00	0.00	0.05	0.04	0.05	0.02	0.04	0.00	0.03	0.04	0.06	0.06
Al_2O_3	20.79	20.82	20.80	19.64	19.77	20.34	19.64	21.34	19.67	19.44	19.47	20.48	19.78	19.94	21.35	19.97	20.47	19.91	20.16	21.00	20.62	19.89	19.74	19.57
Cr_2O_3	0.00	0.02	0.05	0.03	0.00	0.00	0.00	0.00	0.02	0.00	0.02	0.00	0.00	0.00	0.01	0.00	0.01	0.01	0.01	0.00	0.00	0.00	0.04	0.02
FeO	20.49	20.06	21.48	21.42	22.64	20.54	20.84	19.13	22.19	22.28	22.19	20.74	22.39	22.25	18.38	20.89	20.52	22.85	22.65	20.26	24.38	21.85	23.08	22.19
MnO	0.78	0.73	0.79	0.81	0.84	0.91	0.79	0.94	0.73	0.78	0.73	0.80	0.72	0.69	1.03	0.79	0.79	0.76	0.68	0.80	0.78	0.72	0.64	0.77
MgO	17.93	18.01	17.07	17.67	17.06	17.66	18.12	19.43	17.41	17.33	17.31	18.28	16.93	17.25	18.53	17.77	17.25	16.45	16.85	18.68	15.19	17.27	16.51	17.66
CaO	0.01	0.08	0.08	0.00	0.03	0.12	0.04	0.01	0.03	0.06	0.02	0.01	0.02	0.07	0.01	0.07	0.05	0.10	0.07	0.03	0.03	0.02	0.01	0.01
Na_2O	0.02	0.00	0.03	0.01	0.00	0.00	0.00	0.01	0.03	0.00	0.04	0.00	0.02	0.02	0.00	0.00	0.02	0.01	0.00	0.01	0.01	0.03	0.00	0.01
K_2O	0.00	0.00	0.01	0.00	0.01	0.01	0.03	0.02	0.07	0.05	0.00	0.02	0.03	0.06	0.02	0.01	0.04	0.01	0.00	0.01	0.02	0.00	0.01	0.00
Total	86.28	85.98	86.43	86.47	86.84	85.76	86.44	87.39	87.36	87.00	86.34	87.14	86.87	86.99	85.52	86.04	86.02	86.65	86.95	87.89	87.53	86.48	86.56	86.89
Si	5.479	5.495	5.486	5.640	5.562	5.515	5.638	5.429	5.652	5.657	5.599	5.556	5.656	5.593	5.462	5.576	5.623	5.598	5.560	5.545	5.565	5.603	5.596	5.580
Al^{IV}	2.521	2.505	2.514	2.360	2.438	2.485	2.362	2.571	2.348	2.343	2.401	2.444	2.344	2.407	2.538	2.424	2.377	2.402	2.440	2.455	2.435	2.397	2.404	2.420
Ti	0.013	0.005	0.002	0.000	0.011	0.006	0.005	0.006	0.013	0.008	0.008	0.000	0.000	0.000	0.008	0.006	0.008	0.003	0.006	0.000	0.005	0.006	0.010	0.009
Al^{VI}	2.607	2.635	2.636	2.496	2.466	2.573	2.481	2.587	2.481	2.456	2.445	2.557	2.543	2.514	2.720	2.528	2.680	2.549	2.547	2.609	2.674	2.530	2.514	2.419
Cr^{3+}	0.000	0.003	0.008	0.005	0.000	0.000	0.000	0.000	0.003	0.000	0.003	0.000	0.000	0.000	0.002	0.000	0.002	0.002	0.002	0.000	0.000	0.000	0.007	0.003
Fe^{2+}	3.586	3.514	3.774	3.757	3.986	3.624	3.646	3.281	3.866	3.902	3.919	3.594	3.925	3.897	3.212	3.676	3.598	4.032	3.976	3.467	4.286	3.841	4.080	3.893
Mn^{2+}	0.138	0.130	0.141	0.144	0.150	0.163	0.140	0.163	0.129	0.138	0.131	0.140	0.128	0.122	0.182	0.141	0.140	0.136	0.121	0.139	0.139	0.128	0.115	0.137
Mg	5.594	5.624	5.347	5.525	5.354	5.555	5.651	5.941	5.407	5.411	5.450	5.647	5.291	5.385	5.772	5.574	5.391	5.174	5.272	5.698	4.761	5.411	5.203	5.523
Ca	0.002	0.018	0.018	0.000	0.007	0.027	0.009	0.002	0.007	0.013	0.005	0.002	0.004	0.016	0.002	0.016	0.011	0.023	0.016	0.007	0.007	0.005	0.002	0.002
Na	0.008	0.000	0.012	0.004	0.000	0.000	0.000	0.004	0.012	0.000	0.016	0.000	0.008	0.008	0.000	0.000	0.008	0.004	0.000	0.004	0.004	0.012	0.000	0.004
K	0.000	0.000	0.003	0.000	0.003	0.003	0.008	0.005	0.019	0.013	0.000	0.005	0.008	0.016	0.005	0.003	0.011	0.003	0.000	0.003	0.005	0.000	0.003	0.000
Σcations	19.948	19.929	19.941	19.932	19.976	19.951	19.940	19.990	19.935	19.942	19.977	19.946	19.908	19.958	19.903	19.943	19.849	19.926	19.939	19.926	19.881	19.933	19.933	19.991
Fe/(Fe + Mg)	0.391	0.385	0.414	0.405	0.427	0.395	0.392	0.356	0.417	0.419	0.418	0.389	0.426	0.420	0.358	0.397	0.400	0.438	0.430	0.378	0.474	0.415	0.440	0.413
X_c	0.948	0.929	0.927	0.935	0.960	0.930	0.934	0.964	0.927	0.932	0.959	0.941	0.916	0.934	0.913	0.936	0.879	0.920	0.939	0.928	0.902	0.936	0.944	0.973
NIC	19.938	19.911	19.908	19.927	19.967	19.921	19.923	19.979	19.898	19.916	19.956	19.939	19.888	19.918	19.896	19.925	19.819	19.896	19.924	19.913	19.864	19.916	19.929	19.985
IC	0.010	0.018	0.033	0.004	0.009	0.030	0.017	0.011	0.037	0.027	0.021	0.008	0.021	0.040	0.008	0.018	0.030	0.029	0.016	0.013	0.016	0.017	0.005	0.006

IC: interlayerd cations (Ca + Na + K); NIC: non-interlayered cations (Si + Al + Fe + Mg + Mn); X_c: proportion of chlorite in the chlorite/smectite after Wise's method; all Fe assumed to be Fe^{2+}.

Table 4 (*continued*)

Sample	5	5	5	5	10	10	10	10	10	13	13	13	13	13	13	14	8	8	9	9	9	9	9	9	9
Texture	WDefP	WDefP	WDefP	WDefP	WDefP	WDefP	WDefP	WDefP	WDefP	WDefP	WDefP	WDefP	WDefP	WDefP	WDefP	WDefP	WDefP	WDefP	Pcata	Pcata	Pcata	Pcata	Pcata	Pcata	Pcata
Mineral	Chl	Chl	Chl	Chl	Chl	Chl	Chl	Chl	Chl	Chl	Chl	Chl	Chl	Chl	Chl	Chl	Chl	Chl	Chl	Chl	Chl	Chl	Chl	Chl	Chl
SiO_2	26.80	26.77	27.31	26.49	27.01	27.21	26.71	28.16	27.98	26.81	26.76	28.05	26.81	27.03	26.91	26.25	27.03	26.66	27.13	26.71	27.33	26.60	27.37	27.29	27.11
TiO_2	0.02	0.00	0.01	0.00	0.00	0.02	0.05	0.04	0.05	0.02	0.03	0.07	0.01	0.03	0.05	0.02	0.09	0.00	0.03	0.00	0.05	0.02	0.05	0.04	0.03
Al_2O_3	20.48	20.52	20.79	20.12	19.41	20.19	19.70	19.16	18.17	19.71	19.07	18.37	19.44	19.59	19.84	19.92	19.95	19.81	20.53	20.64	20.18	19.99	20.12	20.52	20.76
Cr_2O_3	0.00	0.00	0.03	0.00	0.00	0.00	0.00	0.02	0.01	0.01	0.00	0.02	0.02	0.03	0.00	0.00	0.00	0.03	0.02	0.00	0.00	0.08	0.03	0.01	0.00
FeO	22.78	22.70	22.08	22.18	21.58	21.27	20.99	20.67	21.32	20.72	22.67	21.02	22.40	22.44	21.20	21.93	21.79	21.83	20.14	20.86	20.88	21.17	19.14	20.55	20.03
MnO	0.67	0.68	0.72	0.75	0.74	0.61	0.63	0.65	0.62	0.85	0.76	0.72	0.69	0.78	0.78	0.76	0.68	0.67	0.60	0.49	0.48	0.51	0.60	0.59	0.63
MgO	16.54	17.29	17.90	17.07	17.45	18.12	17.14	17.70	18.80	18.13	17.06	18.92	17.24	17.09	18.03	17.56	17.58	17.60	18.18	17.77	18.32	17.72	19.73	18.51	17.82
CaO	0.07	0.01	0.06	0.06	0.05	0.24	0.04	0.10	0.04	0.03	0.04	0.14	0.10	0.06	0.05	0.10	0.03	0.01	0.11	0.02	0.05	0.05	0.03	0.01	0.04
Na_2O	0.04	0.00	0.01	0.00	0.01	0.02	0.01	0.00	0.01	0.00	0.04	0.01	0.00	0.01	0.00	0.00	0.02	0.02	0.00	0.01	0.03	0.01	0.00	0.02	0.00
K_2O	0.00	0.01	0.01	0.02	0.02	0.02	0.03	0.09	0.02	0.03	0.02	0.03	0.03	0.03	0.03	0.01	0.03	0.02	0.01	0.00	0.03	0.03	0.01	0.00	0.01
Total	87.40	87.98	88.92	86.69	86.27	87.70	85.30	86.59	87.02	86.31	86.45	87.35	86.74	87.09	86.89	86.55	87.20	86.65	86.75	86.50	87.35	86.18	87.08	87.54	86.43
Si	5.591	5.545	5.571	5.566	5.682	5.612	5.664	5.855	5.820	5.617	5.659	5.806	5.637	5.658	5.610	5.525	5.625	5.592	5.619	5.569	5.640	5.587	5.619	5.609	5.628
Al^{IV}	2.409	2.455	2.429	2.434	2.318	2.388	2.336	2.145	2.180	2.383	2.341	2.194	2.363	2.342	2.390	2.475	2.375	2.408	2.381	2.431	2.360	2.413	2.381	2.391	2.372
Ti	0.003	0.000	0.002	0.000	0.000	0.003	0.008	0.006	0.008	0.003	0.005	0.011	0.002	0.005	0.008	0.003	0.014	0.000	0.005	0.000	0.008	0.003	0.008	0.006	0.005
Al^{VI}	2.626	2.555	2.569	2.549	2.495	2.520	2.588	2.550	2.274	2.485	2.412	2.287	2.454	2.490	2.485	2.467	2.519	2.490	2.630	2.641	2.547	2.536	2.487	2.579	2.708
Cr^{3+}	0.000	0.000	0.005	0.000	0.000	0.000	0.000	0.003	0.002	0.002	0.000	0.003	0.003	0.005	0.000	0.000	0.000	0.005	0.003	0.000	0.000	0.013	0.005	0.002	0.000
Fe^{2+}	3.974	3.932	3.767	3.897	3.797	3.669	3.723	3.594	3.709	3.631	4.009	3.638	3.939	3.928	3.696	3.860	3.792	3.830	3.488	3.637	3.603	3.719	3.286	3.532	3.478
Mn^{2+}	0.118	0.119	0.124	0.133	0.132	0.107	0.113	0.114	0.109	0.151	0.136	0.126	0.123	0.138	0.138	0.135	0.120	0.119	0.105	0.087	0.084	0.091	0.104	0.103	0.111
Mg	5.144	5.339	5.443	5.347	5.473	5.572	5.419	5.486	5.830	5.663	5.378	5.838	5.404	5.333	5.603	5.510	5.454	5.504	5.613	5.523	5.636	5.549	6.038	5.671	5.515
Ca	0.016	0.002	0.013	0.014	0.011	0.053	0.009	0.022	0.009	0.007	0.009	0.031	0.023	0.013	0.011	0.023	0.007	0.002	0.024	0.004	0.011	0.011	0.007	0.002	0.009
Na	0.016	0.000	0.004	0.000	0.004	0.008	0.004	0.000	0.004	0.000	0.016	0.004	0.000	0.004	0.000	0.000	0.008	0.008	0.000	0.004	0.012	0.004	0.000	0.008	0.000
K	0.000	0.003	0.003	0.005	0.005	0.005	0.008	0.024	0.005	0.008	0.005	0.008	0.008	0.008	0.008	0.003	0.008	0.005	0.003	0.000	0.008	0.008	0.003	0.000	0.003
Σcations	19.897	19.951	19.929	19.945	19.916	19.937	19.872	19.801	19.949	19.949	19.971	19.947	19.955	19.925	19.949	20.002	19.922	19.963	19.871	19.897	19.909	19.934	19.938	19.903	19.828
Fe/(Fe + Mg)	0.436	0.424	0.409	0.422	0.410	0.397	0.407	0.396	0.389	0.391	0.427	0.384	0.422	0.424	0.397	0.412	0.410	0.410	0.383	0.397	0.390	0.401	0.352	0.384	0.387
X_c	0.908	0.949	0.929	0.935	0.919	0.911	0.900	0.845	0.946	0.938	0.948	0.929	0.937	0.922	0.940	0.965	0.930	0.952	0.895	0.922	0.922	0.936	0.945	0.926	0.879
NIC	19.865	19.946	19.910	19.927	19.896	19.871	19.851	19.755	19.931	19.934	19.940	19.904	19.925	19.899	19.930	19.977	19.899	19.947	19.844	19.888	19.878	19.911	19.929	19.893	19.817
IC	0.032	0.005	0.020	0.019	0.021	0.066	0.021	0.046	0.018	0.015	0.031	0.043	0.031	0.026	0.019	0.025	0.023	0.016	0.027	0.009	0.031	0.023	0.009	0.010	0.012

(*continued on next page*)

Table 4 (continued)

Sample	12	12	16	3	15	15	15	15	15	4	4	4	4	4	7	7	7	7	7	2	2	2	2	2	2
Texture	Pcata	Pcata	Pcata	Pcata	Cata	Cata	Cata	Cata	Cata	Cata	Cata	Cata	Cata	Cata	Cata	Cata	Cata	Cata	Cata	Ucata	Ucata	Ucata	Ucata	Ucata	Ucata
Mineral	Chl	Chl	Chl	Chl	Chl	Chl	Chl	Chl	Chl	Chl	Chl	Chl	Chl	Chl	Chl	Chl	Chl	Chl	Chl	Chl	Chl	Chl	Chl	Chl	Chl
SiO_2	27.32	26.87	26.43	26.52	26.16	27.08	27.03	26.41	26.94	26.87	27.16	26.97	27.03	27.15	26.83	26.58	27.14	27.00	27.21	27.24	28.32	27.67	28.28	26.94	27.02
TiO_2	0.00	0.01	0.03	0.01	0.02	0.04	0.01	0.00	0.05	0.00	0.10	0.05	0.02	0.05	0.03	0.04	0.05	0.09	0.04	0.09	0.04	0.00	0.04	0.08	0.03
Al_2O_3	20.59	20.18	21.01	19.78	20.33	21.13	20.34	20.86	20.12	19.57	20.13	19.51	19.71	20.16	19.82	19.63	19.66	19.13	19.26	20.64	18.80	19.09	18.14	19.89	20.37
Cr_2O_3	0.01	0.01	0.00	0.00	0.06	0.00	0.00	0.02	0.00	0.04	0.06	0.02	0.00	0.00	0.00	0.02	0.04	0.01	0.02	0.00	0.00	0.01	0.00	0.01	0.00
FeO	19.90	19.83	20.02	21.05	23.15	18.57	18.64	19.28	20.36	20.96	21.27	21.35	21.37	21.49	23.33	23.33	23.31	22.03	22.27	18.68	18.69	18.95	18.40	18.54	21.34
MnO	0.56	0.59	0.52	0.70	0.56	0.90	0.75	0.92	0.59	0.66	0.56	0.62	0.70	0.60	0.65	0.56	0.63	0.67	0.68	0.57	0.63	0.63	0.56	0.66	0.59
MgO	18.81	18.40	18.38	18.19	15.69	19.94	19.26	19.25	18.10	17.88	17.48	18.27	17.81	17.57	16.77	16.72	16.74	18.09	17.20	18.86	19.89	19.91	20.67	19.81	17.56
CaO	0.01	0.04	0.03	0.03	0.04	0.06	0.04	0.01	0.02	0.08	0.05	0.08	0.06	0.07	0.18	0.03	0.06	0.05	0.14	0.09	0.16	0.14	0.00	0.01	0.07
Na_2O	0.01	0.02	0.01	0.02	0.01	0.01	0.02	0.00	0.01	0.03	0.01	0.03	0.01	0.03	0.00	0.00	0.03	0.00	0.01	0.00	0.01	0.03	0.00	0.01	0.00
K_2O	0.01	0.00	0.01	0.00	0.02	0.02	0.04	0.00	0.02	0.05	0.01	0.03	0.01	0.07	0.01	0.00	0.00	0.03	0.03	0.15	0.04	0.00	0.00	0.05	0.07
Total	87.22	85.95	86.44	86.30	86.04	87.75	86.13	86.75	86.21	86.14	86.83	86.93	86.72	87.19	87.62	86.91	87.66	87.10	86.86	86.32	86.58	86.43	86.09	86.00	87.05
Si	5.615	5.614	5.495	5.567	5.564	5.507	5.604	5.464	5.626	5.645	5.653	5.624	5.647	5.638	5.606	5.600	5.661	5.642	5.704	5.628	5.832	5.724	5.850	5.595	5.615
Al^{IV}	2.385	2.386	2.505	2.433	2.436	2.493	2.396	2.536	2.374	2.355	2.347	2.376	2.353	2.362	2.394	2.400	2.339	2.358	2.296	2.372	2.168	2.276	2.150	2.405	2.385
Ti	0.000	0.002	0.005	0.002	0.003	0.006	0.002	0.000	0.008	0.000	0.016	0.008	0.003	0.008	0.005	0.006	0.008	0.014	0.006	0.014	0.006	0.000	0.006	0.012	0.005
Al^{VI}	2.602	2.583	2.643	2.460	2.660	2.572	2.574	2.551	2.578	2.491	2.592	2.418	2.500	2.572	2.487	2.475	2.494	2.353	2.462	2.654	2.396	2.379	2.272	2.463	2.604
Cr^{3+}	0.002	0.002	0.000	0.000	0.010	0.000	0.000	0.003	0.000	0.007	0.010	0.003	0.000	0.000	0.000	0.003	0.007	0.002	0.003	0.000	0.000	0.002	0.000	0.002	0.000
Fe^{2+}	3.420	3.465	3.481	3.695	4.118	3.158	3.232	3.336	3.556	3.683	3.703	3.723	3.734	3.732	4.077	4.111	4.066	3.850	3.904	3.228	3.219	3.279	3.183	3.220	3.709
Mn^{2+}	0.097	0.104	0.092	0.124	0.101	0.155	0.132	0.161	0.104	0.117	0.099	0.110	0.124	0.106	0.115	0.100	0.111	0.119	0.121	0.100	0.110	0.110	0.098	0.116	0.104
Mg	5.763	5.731	5.697	5.692	4.975	6.045	5.953	5.937	5.635	5.600	5.424	5.679	5.547	5.439	5.224	5.252	5.205	5.635	5.375	5.809	6.107	6.141	6.374	6.133	5.440
Ca	0.002	0.009	0.007	0.007	0.009	0.013	0.009	0.002	0.004	0.018	0.011	0.018	0.013	0.016	0.040	0.007	0.013	0.011	0.031	0.020	0.035	0.031	0.000	0.002	0.016
Na	0.004	0.008	0.004	0.008	0.004	0.004	0.008	0.000	0.004	0.012	0.004	0.012	0.004	0.012	0.000	0.000	0.012	0.000	0.004	0.000	0.004	0.012	0.000	0.004	0.000
K	0.003	0.000	0.003	0.000	0.005	0.005	0.011	0.000	0.005	0.013	0.003	0.008	0.003	0.019	0.003	0.000	0.000	0.008	0.008	0.040	0.011	0.000	0.000	0.013	0.019
Σcations	19.894	19.903	19.930	19.989	19.885	19.959	19.919	19.991	19.895	19.941	19.860	19.979	19.927	19.903	19.950	19.954	19.917	19.992	19.915	19.864	19.887	19.953	19.933	19.966	19.895
Fe/(Fe + Mg)	0.372	0.377	0.379	0.394	0.453	0.343	0.352	0.360	0.387	0.397	0.406	0.396	0.402	0.407	0.438	0.439	0.439	0.406	0.421	0.357	0.345	0.348	0.333	0.344	0.405
X_c	0.919	0.920	0.939	0.967	0.909	0.941	0.918	0.967	0.918	0.924	0.901	0.954	0.928	0.906	0.929	0.956	0.925	0.970	0.910	0.878	0.892	0.933	0.948	0.956	0.905
NIC	19.885	19.886	19.916	19.974	19.866	19.937	19.891	19.989	19.881	19.898	19.842	19.941	19.907	19.856	19.907	19.947	19.892	19.972	19.872	19.805	19.837	19.910	19.933	19.947	19.861
IC	0.009	0.017	0.013	0.015	0.019	0.022	0.028	0.002	0.014	0.044	0.018	0.038	0.020	0.046	0.043	0.007	0.026	0.019	0.044	0.059	0.050	0.043	0.000	0.019	0.034

Table 5
Major and trace elements from whole-rock XRF analysis (wt.% recalculated to anhydrous base) and measured densities ρ (g/cm^3) of the samples from Caleta Coloso Fault. The average of host rock (HR) composition is represented by sample labeled as "0" (damage zone). Protolith (Proto), weakly deformed protolith (WDefP), protocataclasite (Pcata), cataclasite (Cata) and ultracataclasite (Ucata) were sampled from core zone.

Sample	Damage zone (protolith)						Fault core																		
	49	89	107	139	0	Standard deviation	01	11	06	05	10	13	08	14	091610	09	12	16	03	081609	15	04	07	072108	02
	Host rock	Host rock	Host rock	Host rock	Host rock average		Proto	Proto	Proto	WDefP	WDefP	WDefP	WDefP	WDefP	WDefP	Pcata	Pcata	Pcata	Pcata	Pcata	Cata	Cata	Cata	Cata	Ucata
SiO_2	54.40	57.33	57.22	56.47	56.36	1.36	53.45	58.08	57.41	55.83	56.07	57.22	58.30	58.15	58.06	59.48	61.30	63.82	66.24	56.62	54.48	55.91	58.84	56.12	58.18
TiO_2	0.54	0.40	0.46	0.56	0.49	0.07	0.65	0.33	0.42	0.50	0.55	0.59	0.38	0.50	0.45	0.55	0.49	0.44	0.35	0.59	0.49	0.59	0.44	0.27	0.49
Al_2O_3	18.30	17.60	17.63	18.19	17.93	0.37	19.25	17.58	17.49	18.09	17.83	17.99	18.06	17.81	17.41	17.26	16.53	14.55	14.46	15.57	17.08	18.03	16.90	16.31	17.31
Fe_2O_3	8.04	6.93	6.72	6.89	7.15	0.60	7.98	5.33	6.21	7.06	7.51	6.93	5.82	6.77	6.44	4.98	5.28	4.66	3.82	7.47	7.90	6.33	6.60	6.93	6.08
CaO	7.21	6.83	6.70	6.11	6.71	0.46	5.65	5.54	5.53	5.11	4.43	6.51	5.20	6.25	6.07	6.22	3.36	4.09	5.96	4.39	8.00	5.49	3.89	11.07	5.75
MgO	3.13	2.49	2.47	2.47	2.64	0.33	3.14	1.83	2.42	3.02	3.13	2.01	2.43	2.78	2.83	1.33	2.87	1.54	0.43	3.13	2.38	2.77	2.98	1.00	2.78
MnO	0.20	0.17	0.17	0.15	0.17	0.02	0.16	0.14	0.16	0.17	0.17	0.14	0.16	0.18	0.17	0.13	0.13	0.10	0.10	0.20	0.22	0.14	0.14	0.17	0.17
K_2O	0.87	0.61	0.77	1.15	0.85	0.23	1.14	0.95	1.24	0.84	0.58	0.37	0.36	0.64	0.58	0.57	0.52	1.85	0.06	0.65	0.89	0.63	0.82	0.64	0.55
Na_2O	3.96	4.04	4.03	4.01	4.01	0.04	4.51	5.03	4.85	4.21	5.15	4.26	5.48	4.52	4.19	5.56	5.74	3.26	5.26	4.07	3.27	4.36	4.55	1.80	4.05
P_2O_5	0.17	0.17	0.16	0.17	0.17	0.01	0.18	0.18	0.18	0.20	0.20	0.18	0.18	0.18	0.20	0.23	0.22	0.11	0.13	0.23	0.15	0.19	0.18	0.12	0.12
LOI	1.52	1.10	0.86	2.25	1.43	0.61	3.70	3.66	2.82	4.21	3.55	2.51	2.64	1.69	1.49	2.39	2.87	4.33	1.69	2.59	4.12	4.63	3.89	3.15	3.23
Total	98.34	97.67	97.19	98.42	97.91	0.58	99.81	98.65	98.73	99.24	99.17	98.71	99.01	99.47	97.89	98.70	99.31	98.75	98.50	95.51	98.98	99.07	99.23	97.58	98.71
Ba	239	174	192	325	233	67	226	190	341	125	290	102	139	183	195	118	63	181	64	272	61	991	95	74	171
Rb	16	10	11	19	14	4	23	14	19	13	9	4	5	7	7	9	10	38	n.d.	5	19	12	17	7	10
Sr	466	450	456	459	458	7	497	505	493	470	480	583	518	505	477	469	286	260	462	401	459	516	370	757	481
Zr	140	124	83	149	124	29	117	97	86	135	85	145	75	119	114	121	123	128	93	108	109	111	64	79	90
V	142	119	110	123	124	13	137	81	96	104	109	122	92	107	102	79	64	74	71	135	137	103	108	114	122
Nd	23	15	15	15	17	4	17	17	16	17	19	16	20	24	14	19	17	15	15	14	20	19	21	13	15
Density	2.654	2.685	2.760	2.724	2.706	0.046	2.676	2.663	2.700	2.691	2.666	2.654	2.701	2.720	2.683	2.853	2.808	2.739	2.806	2.719	2.758	2.749	2.706	2.752	2.758

n.d., Not detected.

observed in K_2O reflects the high mobility of this element in fluid–rock interaction processes. Cataclasite show a rather similar pattern than that of the baseline (Fig. 7e) and only the variations in CaO (decreasing and higher dispersion) and LOI (increasing up to 4.63 wt.%) are remarkable. CaO dispersion could be mostly related with the variable epidote/chlorite ratio meanwhile increasing LOI could be associated with pervasive chloritization as described in the petrographic section and summarized in Table 1. The similarity in the geochemical pattern of cataclasite with respect to the baseline could indicate that in geochemical terms, these rocks have a rather close system behavior contrasting with those observed in protocataclasite. Finally, the ultracataclasite sample also fit the general pattern of baseline (Fig. 7f) but Fe_2O_3 and CaO decrease with an increase in LOI associated with the pervasive alteration, grain reduction and abundance of clay minerals in the very fine grained matrix.

In order to determine the extent of chemical mobility related to the hydrothermal alteration in the fault core, we used the quantification method of Gresens (1967), who proposes that the absolute mobility of an element *i* in a natural system can be represented by Eq. (1):

$$\Delta m_i = f_v(\rho_a/\rho_o)C_a^i - C_o^i \quad (1)$$

where Δm_i is the mass change in the component *i*, ρ is the density, o and a correspond to the original and altered rocks, respectively, C represents the concentration (expressed as wt.%) and f_v is the volume factor of the final volume with respect to the initial one. The isocon analysis (Grant, 1986, 2005), based on the method by Gresens (1967), provides a simple and very useful way to quantify gain or loss in mass transfer associated with different geological processes (see Grant, 2005 for a complete review). Isocon diagrams are based on the assumption that at least one element remains immobile during alteration. In a simple binary diagram, plotting unaltered rock against altered rock, elements plotting above the isocon line would be added to the system during alteration, while those plotting below this line would be lost. Elements plotting along the isocon line would be considered as immobile. The most useful expression to calculate the gain or loss of elements during alteration is the change in the concentration of a component (ΔC_a^i) related to its concentration prior to alteration, following the expression proposed by Grant (1986) and given by Eq. (2):

$$\left(\Delta C_a^i/C_o^i\right) = (m_a/m_o)\left(C_a^i/C_o^i\right) - 1 \quad (2)$$

where m_a/m_o is the slope of the line (isocon) from the origin to the data point.

Various software have been published in recent years allowing the easy manipulation of the Grant (1986) and Gresens (1967) equations (e.g. Coelho, 2006; Lopez-Moro, 2012; Potdevin, 1993; Sturm, 2003), enabling the user to plot both isocon and composition–volume diagrams. The most recent (EASYGRESGRANT, Lopez-Moro, 2012) allows the quantification of the absolute mobility of elements using Gresens' (1967) equations, and to draw isocon diagrams (Grant, 1986) that allow mass balance/volume change calculations.

For chemical mobility analysis and mass balance calculations, we consider Zr and Nd as immobile elements based on petrographic relationships. All major elements participate in some way in the different mineral reactions during hydrothermal alteration. For this reason neither Al_2O_3 nor TiO_2 (typical elements considered as immobile in mass balance papers, e.g. Hashimoto et al., 2009) were considered as immobile. On the contrary, the absence of hydrothermal minerals related to exotic fluids (high CO_2 or high halogen-bearing fluids) during alteration suggests that Zr and Nd could be considered as immobile and, consequently, used for the isocon analysis. As previously indicated, we have selected the average of the four tonalite host-rock samples from the damage zone (Table 1) as the baseline and representative of "unaltered" host rock (sample 0 in Table 5, average LOI value 1.43 ± 0.61 wt.%). As shown previously, the partial chloritization of mafic primary minerals and localized patches of albitization of the primary plagioclase is the

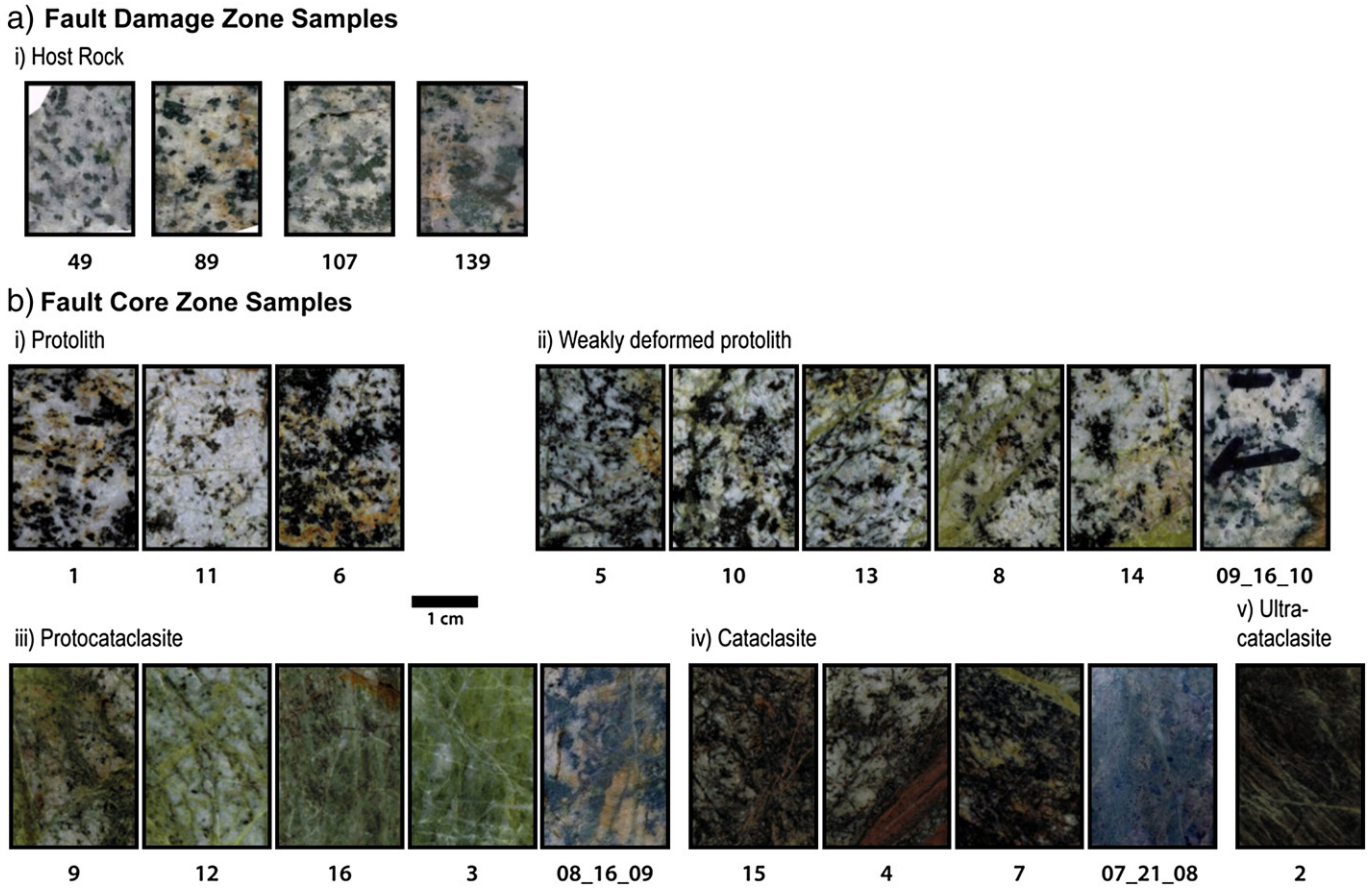

Fig. 4. Representative textures of analyzed samples from damage zone (a) and fault core (b).

only observed hydrothermal alteration. Gain/loss of elements with respect to this sample was calculated using the EASYGRESGRANT algorithm (Lopez-Moro, 2012). Overall volume and mass change (%) were calculated and quoted in Table 6. Both parameters consider the weighted absolute gain/loss volume and mass change for each major element with respect to baseline sample 0. As observed in Table 6, highest overall volume and mass changes are given in those samples with highest SiO_2 and Al_2O_3 variations, because both elements constitute around 75% of the total sample weight. The average of the volume factor (average f_v) for each sample, which is expressed as the ratio of the final volume in the fault rocks from core zone relative to the initial volume in the host rock from damage zone considering all major elements and density of rocks, is given in Table 6. This parameter is an indicator about volume change during alteration. Obtained values close to 1.0 are interpreted as no volume changes meanwhile deviation (positive or negative) from unity is interpreted as volume gain or loss. The final results (expressed as gain/loss relative to the baseline sample 0) are shown in Table 6 and plotted in Fig. 8 by average values and standard deviation of each textural rock.

Fig. 8a shows the chemical mobility observed in samples considered as protolith in the fault core zone. As expected, overall elemental changes are negligible with average values of $\Delta C^i/C^i_o \sim 0$ and only a slight increase in Na_2O and K_2O is observed, likely associated with the low and incipient plagioclase albitization and sericitization. Gain and dispersion in the large ion lithophile elements (LILEs) Rb, Ba and Sr are also related with the high mobility of these elements during alteration processes and as expected, V, Zr and Nd present immobile behavior. In addition, the f_v of these samples is close to 1 ($f_v = 1.15 \pm 0.11$), mainly controlled by minor SiO_2 and Al_2O_3 gain. Consistent with the preservation of igneous textures, no significant chemical changes are observed in samples classified as weakly deformed protolith (Fig. 7b). In this group of samples, a decrease in Na_2O and coupled increase in K_2O are the most remarkable chemical changes. LILEs also show higher variations with loss and gain concomitant with major elements. Broader gain/loss variations in MgO and CaO are mostly related to the variable chloritization degrees of primary amphibole and biotite, plagioclase albitization and sericitization. f_v-values for these samples are close to 1.0, but with higher dispersion than protolith rocks ($f_v = 1.07 \pm 0.15$). Protocataclasites exhibit the highest element (major and trace) gain and loss variations, with the highest dispersion and more different patterns with respect to host rock (Fig. 8c). Nevertheless, these samples show the lowest f_v ($f_v = 1.06 \pm 0.12$) because minor changes in SiO_2 and Al_2O_3 are observed. The highest Fe_2O_3, MnO, MgO and CaO loss (more negative $\Delta C^i/C^i_o$ in Table 6) are related to the highly propylitic alteration observed in these rocks.

Cataclasites have similar chemical pattern to that of the host rock, with average $\Delta C^i/C^i_o \sim 0$ for most elements, but with broader variation range (Fig. 8d). Dispersion in highly mobile elements (CaO, Na_2O and K_2O) is observed in relation to the albite/sericite proportion present in these rocks and the relative increase in FeO and MgO could be related to the higher chlorite content. In concordance with alkaline element mobility, Rb and Ba show high dispersion, having Ba as the highest observed variation range. Average f_v (1.19 ± 0.23) is mostly constrained by the low SiO_2 and Al_2O_3 variations. In contrast with protocataclasite, no major average changes in Fe_2O_3, MnO, MgO and CaO have been observed.

The ultracataclasite sample shows the highest absolute overall mass and volume changes (26% and 23%, respectively), with $\Delta C^i/C^i_o < 0.5$ (Fig. 8e) and the highest average f_v ($f_v = 1.23 \pm 0.12$). These highest values are controlled by the high variation in most of the major

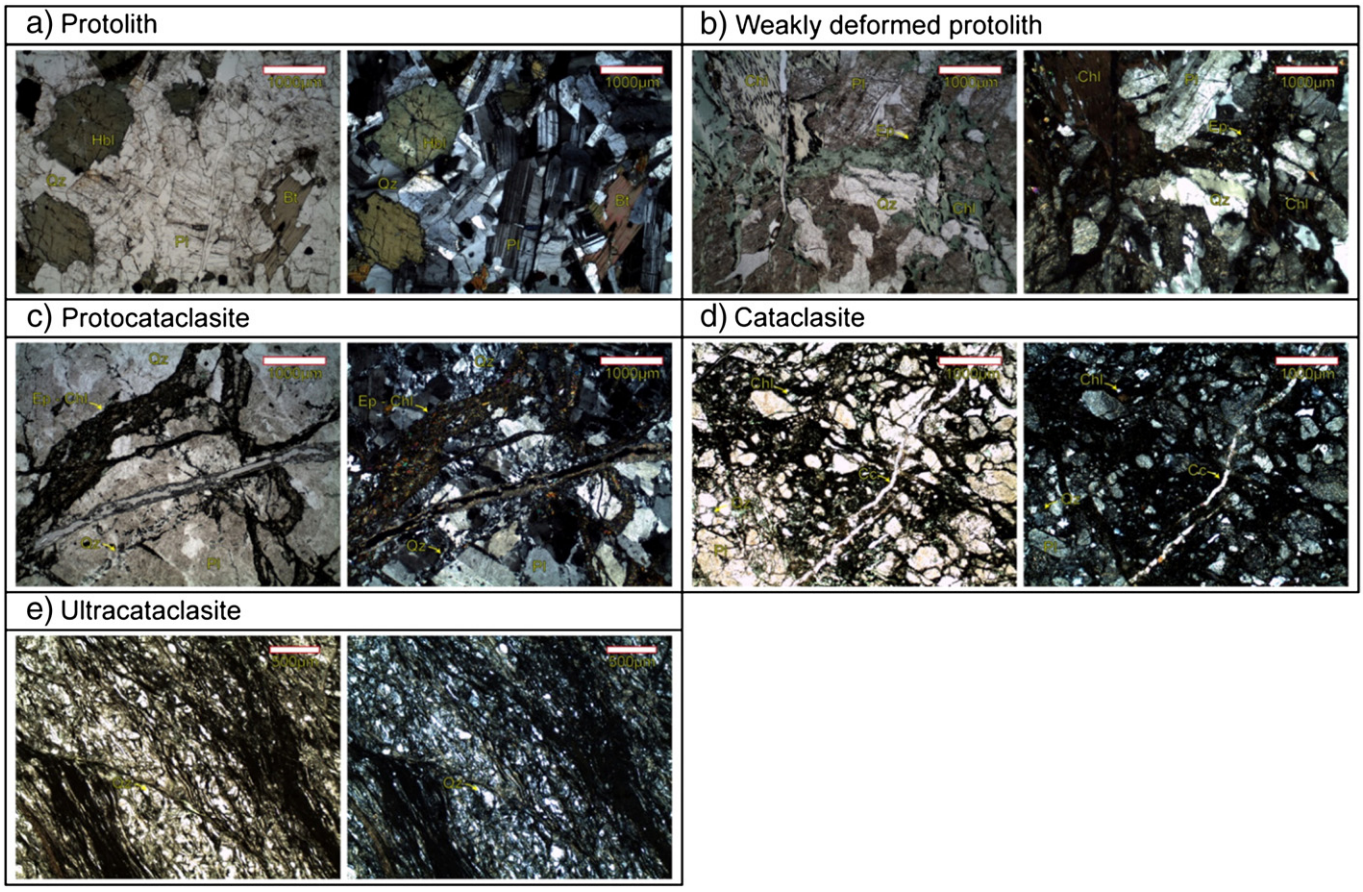

Fig. 5. Microstructures in the Caleta Coloso Fault core rocks (parallel and crossed nicols). (a) Protolith, (b) weakly deformed protolith, (c) protocataclasite, (d) cataclasite, (e) ultracataclasite.

elements, but only one sample was available to this study and consequently conclusions about this rock type must be carefully considered.

5. Discussion

5.1. Tonalitic host-rock P–T emplacement conditions

The Cerro Cristales tonalite originates from the Jurassic magmatic arc emplaced into a thinner continental crust due to the subduction of the Nazca Plate under the South American Plate. The preservation of primary compositions in this rock allows the use of a calibration that can establish the P–T conditions of crystallization. Thus, the presence of the buffer association allows pressure estimations based on the Al–In-hornblende barometry (Schmidt, 1992), obtaining values of 320 to 390 MPa. Assuming a lithostatic pressure gradient of 30 MPa/km, the emplacement depth obtained with this calibration would be around 10 to 13 km.

Temperature values were obtained by using the plagioclase–amphibole thermometer proposed by Blundy and Holland (1990). Using EMPA data from fresh unaltered plagioclase in equilibrium with amphibole, T values of 724 to 745 °C were obtained. This temperature range is consistent with magmatic crystallization values for this kind of evolved rock.

5.2. Hydrothermal alteration conditions

Chloritic and propylitic alteration observed in both host rock and deformed rocks is consistent with low-grade metamorphic conditions during cataclastic processes with fluids at near-neutral pH conditions, as corroborated by the presence of calcite. Variable f_{O2} could also be proposed based on the Fe↔Al substitution observed in epidote.

Determination of P–T conditions related to this kind of very low-grade alteration processes is difficult, based on the absence of precise geothermobarometer that could be applied to such low-temperature processes. Different calibrations have been proposed using chlorite composition for calculating temperature (see Caritat et al., 1993). Many studies have been critical of the use of chlorite composition alone as a geothermometer due to the absence of a thermodynamic basis for these calibrations. In addition, smectite layers within the chlorite structure could potentially influence the Al content, and consequently the calculated temperatures (Essene and Peacor, 1995). Moreover, some of the Fe in chlorite could exist as Fe^{3+} (Miyahara et al., 2005), where the total number of octahedral cations exceeds 12 a.p.f.u. This underestimation of the Fe^{3+} abundances affects the estimation of the smectite ratio and, consequently, the use of chlorite as geothermometer (Miyahara et al., 2005). Additionally, higher IC (interlayered cations) values (>0.1) would indicate the presence of a discrete phase in the chlorite aggregates and, consequently, the whole-rock chlorite composition would not be suitable as geothermometer (Miyahara et al., 2005). However, chlorites formed during hydrothermal alteration in the different fault rocks of the Caleta Coloso Fault core are characterized by a rather homogeneous chemical signature, with chlorites from each fault rock type having a very similar compositional range independent of the deformational textures. Additionally, the total number of octahedral cations never exceeds 12, excluding the possibility of underestimating Fe^{3+} and validating the calculation of the chlorite/smectite ratio based on chemical analyses. An average X_c (smectite to chlorite ratio) of 0.923 (range from 0.973 to 0.845) indicates a high chlorite content in the mafic phyllosilicate structure with a

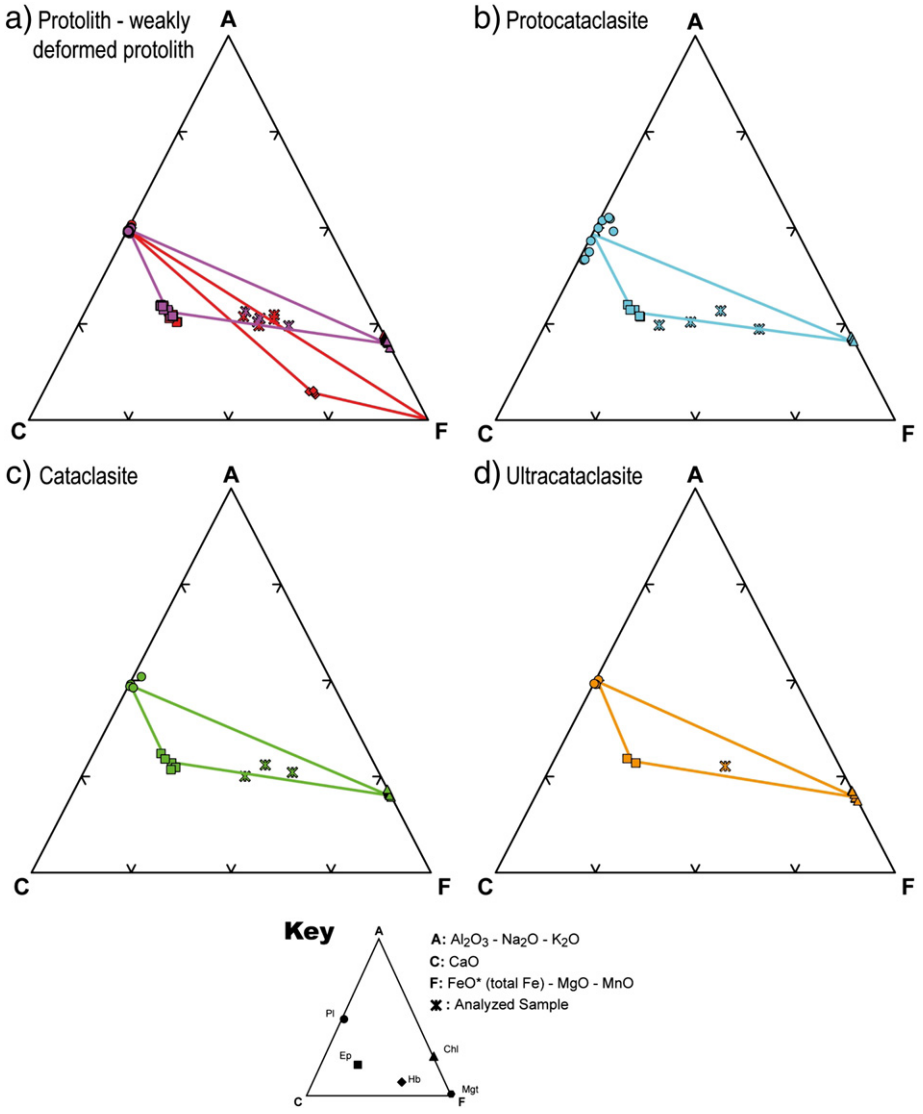

Fig. 6. Ternary ACF diagrams (in molar proportions) of the (a) protolith (red) and weakly deformed protolith (purple), (b) protocataclasite (cyan), (c) cataclasite (green) and (d) ultracataclasite (orange). A: Al_2O_3–Na_2O–K_2O; C: CaO, F: FeO* (total Fe) + MgO + MnO. Pl: plagioclase (circle), Hb: hornblende (rhombus), Ep: epidote (square), Chl: chlorite (triangle), and Mgt: magnetite.

very low amount of interlayered cations (IC from 0.066 to 0.000 a.p.f.u.) and with a rather homogeneous compositional range. All these chemical characteristics would suggest the use of chlorite composition as valid for geothermometry. Furthermore, the chemical chlorite composition homogeneity is coupled with only slight zonation observed in epidote.

The application of the empirical chlorite geothermometer (Cathelineau, 1988), based on the tetrahedral Al occupancy in chlorite, indicates a temperature of mineral formation in a range of 284 to 352 °C (average of 323 °C) for the protolith, weakly deformed protolith, protocataclasite, cataclasite and ultracataclasite (Fig. 9). Lower temperature values were obtained from those chlorite analyses with higher smectite ratio ($X_c = 0.845$), while the highest obtained figures belong to almost pure chlorites with very low smectite layers ($X_c = 0.973$). This temperature range is the same when Jowett's (1991) calibration is used and is around 140 to 160 °C lower than the Kranidiotis and MacLean's calibration (Kranidiotis and MacLean, 1987). Independently of the validity of this T-calibration based exclusively on one mineral chemical composition, T values obtained using Cathelineau's (1988) calibration are consistent with the expected conditions for the deformational textures observed in these rocks, and with the most important observation, that there are no differences in the temperature values for the five texturally-different fault rock classifications.

5.3. Chemical mobility

The mass balance and volume variation calculations are consistent with elemental chemical mobility that is predominantly controlled by mineral reactions and cataclasis evolution. Most of the fault core rocks show a decrease in CaO coupled with an increase in Na_2O. This Ca↔Na exchange is mostly related to the partial/total albitization of plagioclase with the consistent Ca release allowing epidote (and calcite) formation and a subsequent volume change. On the other hand, slight increase in SiO_2 observed in most of the fault core rocks (higher in protocataclasite) may be the result of an increase in fracturing during cataclastic deformation. The variable K_2O content observed may have resulted from the partial/total biotite chloritization and/or the variable sericite/chlorite ratio observed, controlled by local fluid–rock conditions. The increase in LOI in rocks from the core zone with respect to host rock (damage zone) is a good parameter of alteration degree, cataclasites having the highest LOI values in which a pervasive chloritic alteration is observed (Fig. 7).

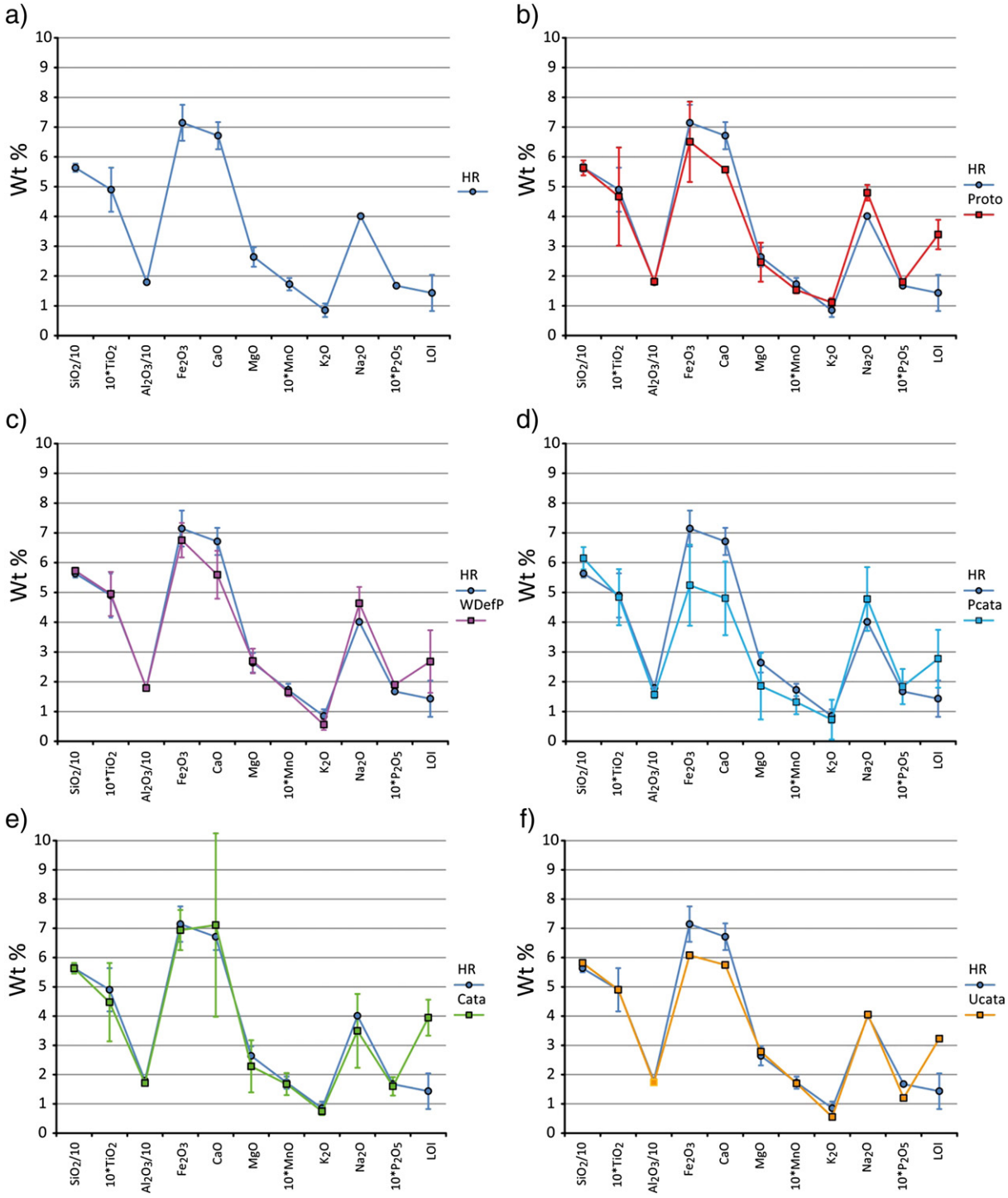

Fig. 7. Major and trace elements from the Caleta Coloso Fault and their dispersion with respect to the baseline: (a) host rock (HR), (b) protolith (Proto), (c) weakly deformed protolith (WDefP), (d) protocataclasite (Pcata), (e) cataclasite (Cata) and (f) ultracataclasite (Ucata).

The new formed hydrothermal alteration mineralogy (mostly composed by chlorite, albite, epidote, quartz and minor calcite) must be explained by local fluid circulation with minor transport of elements. No mineralogical evidences are observed that could support the existence of "exotic" fluids to the primary system. Moreover, the variability in bulk rock composition observed could be explained by the different veinlet/rock ratios rather than for the presence of exotic fluids or high transport distances. Regarding volume changes, obtained f_v-values (Table 6) are strongly conditioned by the variation in the more abundant SiO_2 and Al_2O_3 oxides. Small variations in these two elements imply important mass and volume changes and high mobility of minor elements could be then hid. This fact is especially relevant for the case of protocataclasite. As shown in Figs. 7 and 8, higher dispersion and variability of major and trace elements were obtained in these rocks, but f_v calculated (Table 6) was the lowest because of relatively low SiO_2 and Al_2O_3 variations. These chemical variations observed in protocataclasites could be associated with the first stage of cataclastic deformation, which is characterized by relatively low fracture density but with high dilatancy and enhanced permeability (e.g. Mitchell and Faulkner, 2009), prior to strain localization and extended grain-size reduction and increased packing. Under these conditions,

Table 6
Volumetric changes by isocon analysis, using sample "0" as fresh and undeformed host rock (baseline). Texture of rocks from Caleta Coloso Fault core is indicated: protolith (Proto), weakly deformed protolith (WDefP), protocataclasite (Pcata), cataclasite (Cata) and ultracataclasite (Ucata).

Gain/loss relative to C_i^0 $\Delta C_i/C_i^0$														
Sample	1/0	6/0	11/0	Proto average n = 3	Standard deviation	5/0	10/0	13/0	14/0	8/0	091610/0	WDefP average n = 6	Standard deviation	9/0
Texture	Proto	Proto	Proto			WDefP	WDefP	WDefP	WDefP	WDefP	WDefP			Pcata
SiO_2	−0.02	0.28	0.17	0.14	0.15	−0.05	0.17	−0.03	−0.10	0.29	0.19	0.08	0.16	0.01
TiO_2	0.37	0.07	−0.23	0.07	0.30	−0.02	0.32	0.15	−0.11	−0.03	0.06	0.06	0.15	0.08
Al_2O_3	0.11	0.22	0.12	0.15	0.06	−0.03	0.17	−0.04	−0.13	0.26	0.12	0.06	0.15	−0.08
Fe_2O_3	0.15	0.09	−0.15	0.03	0.16	−0.05	0.24	−0.07	−0.17	0.02	0.04	0.00	0.14	−0.33
MnO	−0.13	0.03	−0.06	−0.05	0.08	−0.27	−0.22	−0.07	−0.19	−0.03	0.13	0.02	0.16	−0.11
MgO	0.22	0.15	−0.21	0.05	0.23	0.10	0.40	−0.27	−0.08	0.15	0.23	0.09	0.23	−0.52
CaO	−0.04	0.16	−0.08	0.01	0.13	−0.05	0.16	−0.22	−0.09	0.16	0.04	−0.12	0.12	−0.28
Na_2O	0.38	0.83	0.27	0.49	0.29	−0.05	−0.20	−0.58	−0.34	−0.47	−0.21	−0.31	0.19	−0.36
K_2O	0.16	0.51	0.43	0.37	0.19	0.01	0.51	0.02	−0.01	0.71	0.20	0.24	0.30	0.33
P_2O_5	0.11	0.35	0.22	0.23	0.12	0.15	0.41	0.03	−0.06	0.35	0.37	0.21	0.20	0.32
Rb	0.69	0.70	0.14	0.51	0.32	−0.11	−0.24	−0.73	−0.56	−0.55	−0.42	−0.44	0.23	−0.38
Ba	0.00	0.83	−0.07	0.25	0.50	−0.49	0.46	−0.58	−0.31	−0.25	−0.04	−0.20	0.38	−0.51
Sr	0.12	0.35	0.26	0.24	0.12	−0.02	0.23	0.22	−0.04	0.42	0.20	0.17	0.17	−0.02
V	0.14	−0.03	−0.26	−0.05	0.20	−0.20	0.03	−0.06	−0.24	−0.07	−0.05	−0.10	0.10	−0.39
Zr	−0.03	−0.13	−0.11	−0.09	0.05	0.04	−0.19	0.12	−0.16	−0.24	0.06	−0.06	0.15	−0.06
Nd	0.03	0.18	0.14	0.12	0.08	−0.04	0.32	−0.10	0.24	0.47	−0.05	0.14	0.24	0.07
Overall mass change (%)	2.99	25.22	13.92	14.04	11.12	−4.07	17.68	−4.12	−12.48	25.17	16.09	7.04	15.30	−4.02
Overall volume change (%)	4.15	25.48	15.75	15.13	10.68	−3.53	19.43	−2.23	−12.93	25.42	15.10	6.21	15.05	−8.96
Average f_v	1.04	1.25	1.16	1.15	0.11	0.96	1.19	0.98	0.87	1.25	1.16	1.07	0.15	0.91
Std f_v	0.03	0.19	0.14	0.12	0.08	0.04	0.29	0.11	0.17	0.40	0.06	0.18	0.14	0.06

fluid–rock interaction processes could be favored and major chemical changes of the more mobile elements produced. On the other hand, cataclastic rocks are characterized by higher fracture density, reduced grain size and filling of previously open spaces by secondary minerals (mainly chlorites). Ultracataclasite represents the extreme grain size reduction and mineral mechanical mixing, dramatically reducing the permeability (e.g. Crawford et al., 2008; Zhang and Tullis, 1998; Zhang et al., 1999) and acting, together with cataclasite, as a barrier for subsequent fluid–flow interaction and chemical mobility.

A conceptual model for fault zone structure involves strain that is localized in a narrow simple fault core surrounded by a distributed zone of fractures and faulting in the damage zone (e.g. Punchbowl Fault, Chester et al., 2005; San Gabriel Fault, Evans and Chester, 1995; San Jacinto Fault, Morton et al., 2012; Cooper Basin Fault, Colby and Girty, 2013). However, a complex structure can be observed where the fault core may branch, anastomose and link lenses of fractured protolith between high-strain material strands, generating a wide multiple-core zone (e.g. Carboneras Fault, Faulkner et al., 2003; Caleta Coloso Fault, Cembrano et al., 2005 and Mitchell and Faulkner, 2009). This multiple core apparently would be product of amalgamation of subsequent individual deformational bands (e.g. Faulkner et al., 2008).

Internal structure of Coloso Fault core, consisting of alternate layers of cataclasite/ultracataclasite and low strain domains, corresponds to a wide fault core zone with multiple cores. This structure fault interpretation would been influenced by precipitation hardening of the fault zone leading to strengthening and subsequent failure along a new plane parallel to the fault zone (e.g. Cembrano et al., 2005; Faulkner et al., 2008).

In the case of simple core architecture, geochemical signature of every type of rocks could be similar and small geochemical variation should be expected into each kind of fault rocks. On the contrary, in multiple core architecture, each band could have characteristic fluid/rock ratio intensities conducting short-distance element transport that should be different for the adjacent band. Consequently, low-strain and high-strain strands of every deformational band could have geochemical signatures and evidence different geochemical mobility from other low-strain and high-strain rocks. As shown in Figs. 7 and 8, we observed that into protocataclasites and cataclasites a considerable dispersion of data occurs and no coherent element behavior has been observed, with variable overall mass and volume changes and random gain/loss of mobile elements. This fact could be interpreted as consequence of local chemical mobility associated with episodic and discrete deformational bands which is in concordance with mechanical development proposed to the Coloso Fault (e.g. Cembrano et al., 2005; Faulkner et al., 2008).

5.4. Proposed model

After the emplacement of the Jurassic tonalite at medium crustal levels (10 to 13 km depth), these rocks underwent brittle cataclastic deformation and associated hydrothermal alteration, likely during the exhumation process. Homogeneity in the alteration mineralogy and temperatures obtained (based on the empirical chlorite calibration) also favors the hypothesis of hydrothermal fluids without great traveling distance and mostly concentrated in the fault core zone. Average $T_{chlorite}$ values obtained at 323 °C could be useful to constrain the maximum depth of faulting. Assuming thermal gradients between 40 and 50 °C/km, figures in concordance with active magmatic arcs, maximum faulting depths would be around 6–8 km.

As indicated by Faulkner et al. (2010) and Mitchell and Faulkner (2009), fault zones in low-porosity rocks are likely to be characterized by a fine-grained fault core surrounded by a fracture-dominated damage zone. This is indeed not the pattern observed in the Caleta Coloso Fault zone, dominated by discrete deformation along fine-grained bands (the cataclasite and ultracataclasite), surrounded by wider fracture-dominated areas of protocataclasite and relics of protolith in the fault core. In the damage zone, fractures would range from micro- to macro-scale accommodating the brittle deformation. Moreover, relatively low alteration observed in host rocks from damage zone would confirm the main fluid flow processes concentrated in the fault core. On the contrary, the intense and pervasive alteration observed in the fault core, with intense propylitic and chloritic alteration, indicates a concentrated high flux of hydrothermal fluids. Because the Coloso Fault zone is developed in an active magmatic arc, the origin of these hydrothermal fluids in depth could be related to the Andean Mesozoic magmatic activity, with high geothermal gradients allowing devolatilization of magmatic products enhancing fluid movements (Faulkner et al., 2008).

12/0	16/0	3/0	081609/0	Pcata average n = 5	Standard deviation	7/0	4/0	15/0	072108/0	Cata average n = 4	Standard deviation	2/0
Pcata	Pcata	Pcata	Pcata			Cata	Cata	Cata	Cata			Ucata
0.09	0.19	0.45	0.19	0.19	0.16	0.43	0.00	−0.04	0.43	0.21	0.26	0.30
0.00	−0.06	−0.12	0.42	0.07	0.21	0.23	0.21	−0.01	−0.21	0.06	0.21	0.26
−0.07	−0.15	−0.01	0.03	−0.06	0.07	0.29	0.01	−0.05	0.31	0.14	0.19	0.21
−0.26	−0.31	−0.34	0.23	−0.20	0.25	0.27	−0.11	0.10	0.40	0.16	0.22	0.07
−0.50	−0.36	0.10	0.37	−0.17	0.30	−0.20	−0.18	0.18	0.42	0.15	0.26	0.08
0.09	−0.39	−0.80	0.40	−0.24	0.48	0.55	0.06	−0.10	−0.46	0.01	0.42	0.32
−0.24	−0.39	−0.29	−0.23	−0.22	0.23	0.11	−0.18	0.27	1.37	0.29	0.74	0.24
−0.39	1.29	−0.91	−0.10	−0.09	0.83	0.33	−0.25	0.04	0.08	0.05	0.24	−0.19
0.44	−0.15	0.62	0.20	0.29	0.29	0.56	0.09	−0.19	−0.35	0.03	0.40	0.27
0.32	−0.31	−0.04	0.62	0.18	0.36	0.48	0.14	−0.11	0.03	0.13	0.25	−0.10
−0.28	1.85		−0.58	0.15	1.14	0.67	−0.14	0.35	−0.28	0.15	0.44	−0.10
−0.73	−0.18	−0.66	0.38	−0.34	0.45	−0.44	3.28	−0.74	−0.54	0.39	1.93	−0.08
−0.37	−0.40	0.24	0.03	−0.10	0.28	0.11	0.13	0.00	1.38	0.40	0.65	0.32
−0.48	−0.37	−0.29	0.29	−0.25	0.31	0.20	−0.16	0.10	0.32	0.11	0.21	0.24
0.00	0.08	−0.08	0.03	−0.01	0.07	−0.29	−0.10	−0.13	−0.08	−0.15	0.10	−0.09
0.00	−0.07	0.09	−0.03	0.01	0.07	0.70	0.12	0.17	0.10	0.27	0.28	0.11
0.41	5.10	23.33	17.56	5.62	12.39	37.35	0.59	−0.62	41.46	18.83	23.83	25.56
−3.25	3.85	18.92	18.12	8.59	11.69	37.37	−1.00	−2.50	43.87	20.30	23.61	23.18
0.97	1.04	1.19	1.18	1.06	0.12	1.37	0.99	0.98	1.41	1.19	0.23	1.23
0.00	0.08	0.10	0.03	0.05	0.04	0.56	0.11	0.14	0.13	0.24	0.22	0.12

The varying degrees of fracture damage and grain-size reduction between the fault core and the damage zone will strongly control the fluid–flow properties of the fault zone. Through mass-balance and volume-change modeling, we have documented different volume changes for the different deformational stages. A schematic model for the chemical mobility related to hydrothermal fault-related fluid–flow circulation observed in the Caleta Coloso Fault core zone is shown in Fig. 10. Rocks classified as protolith are characterized by only slight alteration and no major chemical mobility or volume changes. The very low fluid–flow ratio in this unit is controlled by the low porosity of the undeformed tonalite. Alteration could only take place in microfractures which are observed at thin-section scale. However, as the core zone is approached, the tonalite becomes more altered and newly opened fractures, allowing fluid circulation, start to be more common. This portion of the fault zone shows relatively high volume changes and notable chemical mobility. Protocataclasites have a low to medium fracture density, allowing the higher chemical mobility as shown in Figs. 7 and 8. Moreover, the protocataclasite is also characterized by passive epidote enrichment (with respect to chlorite) in high-strain areas. Finally, with fracturing and comminution, the fluid–rock ratio increases allowing a higher reactive contact surface area. Consequently, the highest fracture density would then be located at the edge of ultracataclasite bands, having a different range of permeability, which is consistent with the proposed model of Mitchell and Faulkner (2012). The higher chlorite content in cataclasite and ultracataclasite with respect to protocataclasite, together with grain size reduction during cataclasis (extreme in ultracataclasite), would act as a barrier for fault-related fluid–flow processes (Fig. 10).

The internal structure complexity observed in the Caleta Coloso Fault core with metric (to decimetric) bands of highly deformed and weakly deformed rocks would constrain the fault-related fluid–flow and associated hydrothermal alteration. Fault zones could act as a fluid–flow conduit but internal complexity can result in intricate structures with differential low- and high-permeability zones. Moreover, highly deformed rocks (cataclasite and ultracataclasite) characterized by extreme grain-size reduction and higher proportion of phyllosilicates (chlorite) would have lower permeability than protocataclasite (e.g. Crawford et al., 2008; Zhang and Tullis, 1998; Zhang et al., 1999), acting as a real barrier for fluid–flow and fluid-driven chemical-mobility reactions and producing a zone of very high permeability anisotropy. In contrast, the weakly deformed rocks would act as an efficient conduit for hydrothermal fault-related fluid–flow. In this case, due to the low initial porosity of tonalite, permeability would be mostly controlled by fractures (Balsamo et al., 2010) and chemical mobility would be more effective conforming the connectivity of the macro-scale fracture network (Faulkner et al., 2010).

Our proposed model for the Caleta Coloso Fault (Fig. 10c) is mostly controlled by precipitation hardening of the fault zone leading to strengthening and subsequent failure along a new plane parallel to the fault zone, following models developed by Faulkner et al. (2008, 2010). Rapid precipitation of hydrothermal minerals could harden a discrete deformational band avoiding stress propagation favoring slip concentration in another discrete deformational band. This heterogeneous strain distribution, with much localized planes of comminution, typically confined to the edges of the strands of cataclasite (Faulkner et al., 2008) is consistent with the random chemical mobility observed in the protocataclasites. Highest chemical dispersion observed in these rocks would be then a consequence of different fluid/rock ratios acting during the discrete strain conditions governing this deformational stage. This model is consistent with the notion of strengthening of cataclasite layers due to mineral precipitation, with later movements accommodated on new fault gouge strands confined to the boundary of the strengthened old cataclasite layers proposed by Faulkner et al. (2008).

6. Conclusions

The Caleta Coloso Fault zone is a major structure in the Atacama Fault Zone, where brittle deformation in Jurassic tonalite resulted in the fault core protocataclasites, cataclasites and discrete band of ultracataclasite, with some unaltered protolith and weakly deformed protolith bands are still present. The fault core is also characterized by intense hydrothermal alteration, whereas host rocks in the damage zone evidence only weak alteration.

Hydrothermal alteration associated with fault-related fluid–flow is characterized by a very low-grade association composed by chlorite, epidote, albite, quartz and calcite. The application of chlorite thermometry indicates T-values in the range of 284 to 352 °C (average temperature of

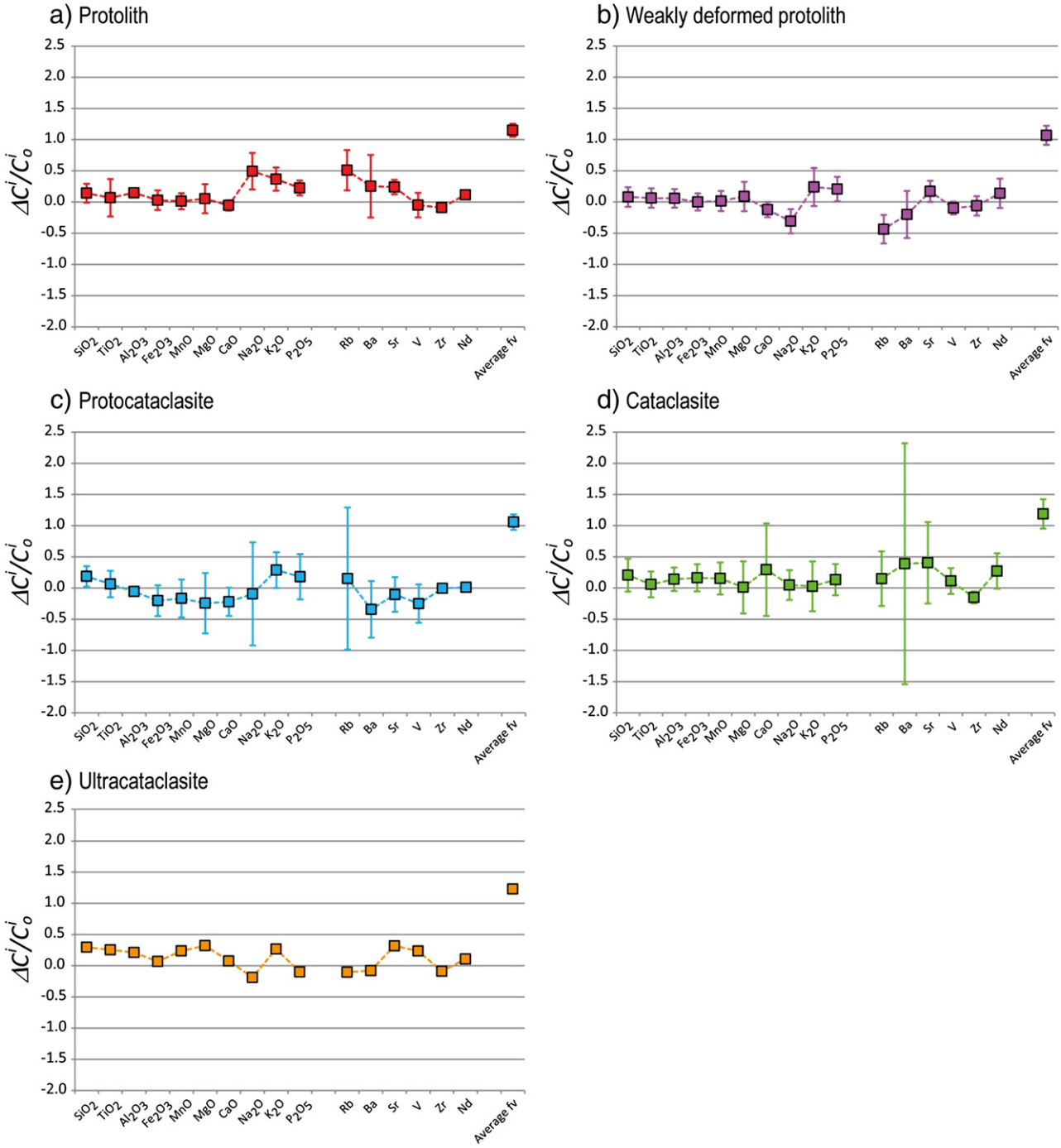

Fig. 8. Chemical mobility of major elements and selected trace elements (expressed as $\Delta C^i/C^i_o$) observed in the different rock types from the Caleta Coloso Fault core. All diagrams were plotted using sample 0 (=average of 4 samples from damage zone) as representative of unaltered rock (baseline). Average of volume factor (f_v) is shown. Errors bars show standard deviation of sample average. (a) Protolith (Proto), (b) weakly deformed protolith (WDefP), (c) protocataclasite (Pcata), (d) cataclasite (Cata) and (e) ultracataclasite (Ucata).

323 °C), indicating maximum depth of faulting between 6 and 8 km. No differences in mineral composition or T-values were observed among different cataclastic rock types, indicating spatially rather homogeneous hydrothermal alteration.

Mass balance and volume change calculations document the major chemical mobility observed in protocataclasite, whereas cataclasite shows smaller changes. This suggests that fluid–flow and chemical alteration were strongly controlled by deformation. Because the protocataclasite was relatively permeable and the cataclasite (and ultracataclasite) acted as a barrier for fluid–flow having a very low permeability due to extreme grain size reduction during cataclasis, differential chemical mobility is observed between them.

Fault zones must be considered as complex and heterogeneous systems, with areas of high permeability that alternate with very low permeability bands. The amalgamation of subsequent and sub-parallel deformation bands is mostly controlled by precipitation hardening of the fault zone leading to strengthening and subsequent failure along a new plane parallel to the fault zone. Chemical mobility and volume changes in these fault zones are consequently mostly controlled

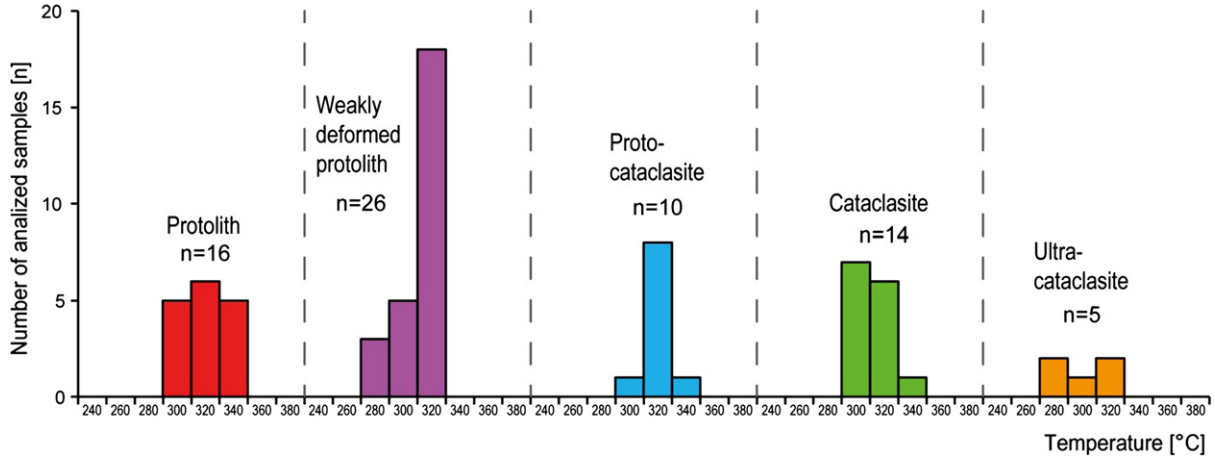

Fig. 9. Histograms of temperatures calculated based on the chlorite Cathelineau (1988) geothermometer for the protolith (red), weakly deformed protolith (purple), protocataclasite (cyan), cataclasite (green) and ultracataclasite (orange).

by the different effective fluid/flow ratios that finally control the fracture–channeling allowing fault-related fluid–flow.

Acknowledgments

This study was funded by FONDECYT project 1100464 and it is a contribution to the FONDAP-CONICYT project 15090013. Corrections and suggestions by the referees and editor highly improved the original version.

References

Balsamo, F., Storti, F., Salvini, F., Silva, A., Lima, C., 2010. Structural and petrophysical evolution of extensional fault zones in low-porosity, poorly lithified sandstones of the Barreiras Formation, NE Brazil. J. Struct. Geol. 32, 1806–1826.

Bettison, L.A., Schiffman, P., 1988. Compositional and structural variations of phyllosilicates from the Point Sal ophiolite, California. Am. Mineral. 73, 62–76.

Bettison-Varga, L., Mackinnon, I.D.R., Shiffman, P., 1991. Integrated TEM, XRD and electron microprobe investigation of mixed-layer chlorite–smectite from the Point Sal ophiolite, California. J. Metamorph. Geol. 9, 697–710.

Bevins, R.E., Robinson, D., Rowbotham, G., 1991. Compositional variations in mafic phyllosilicates from regional low-grade metabasites and application of the chlorite geothermometer. J. Metamorph. Geol. 9, 711–721.

Blundy, J.D., Holland, T.J.B., 1990. Calcic amphibole equilibria and a new amphibole–plagioclase geothermometer. Contrib. Mineral. Petrol. 104, 204–224.

Caritat, P., Hutcheon, I., Walshe, J.L., 1993. Chlorite geothermometry: a review. Clay Clay Miner. 41, 219–239.

Cathelineau, M., 1988. Cation site occupancy in chlorites and illites as a function of temperature. Clay Miner. 23, 471–485.

Cembrano, J., Gonzalez, G., Arancibia, G., Ahumada, I., Olivares, I., Herrera, V., 2005. Fault zone development and strain partitioning in an extensional strike-slip duplex: a case study from the Mesozoic Atacama Fault System, Northern Chile. Tectonophysics 400, 105–125.

Chester, J.S., Chester, F.M., Kronenberg, A.K., 2005. Fracture surface energy of the Punchbowl Fault, San Andreas System. Nature 437, 133–136.

Coelho, J., 2006. GEOISO —a Windows™ program to calculate and plot mass balances and volume changes occurring in a wide variety of geologic processes. Comput. Geosci. 32, 1523–1528.

Colby, T.A., Girty, G.H., 2013. Determination of volume loss and element mobility patterns associated with the development of the Copper Basin fault, Picacho State Recreation Area, SE California, USA. J. Struct. Geol. 51, 14–37.

Cortes, J., Gonzalez, G., Binnie, S.A., Robinson, R., Freeman, S., Vargas, G., 2012. Paleoseismology of the Mejillones Fault, Northern Chile: insights from cosmogenic Be-10 and optically stimulated luminescence determinations. Tectonics 31. http://dx.doi.org/10.1029/2011TC002877 (TC2017).

Crawford, B.R., Faulkner, D.R., Rutter, E.H., 2008. Strength, porosity, and permeability development during hydrostatic and shear loading of synthetic quartz–clay fault gouge. J. Geophys. Res. Solid Earth 113. http://dx.doi.org/10.01029/02006JB004634 (B03207).

Essene, E.J., Peacor, D.R., 1995. Clay mineral thermometry — a critical perspective. Clay Clay Miner. 43, 540–553.

Evans, J.P., Chester, F.M., 1995. Fluid–rock interaction in faults of the San-Andreas system — inferences from San-Gabriel fault rock geochemistry and microstructures. J. Geophys. Res. Solid Earth 100, 13007–13020.

Faulkner, D.R., Lewis, A.C., Rutter, E.H., 2003. On the internal structure and mechanics of large strike-slip fault zones: field observations of the Carboneras Fault in southeastern Spain. Tectonophysics 367 (3–4), 235–251.

Faulkner, D.R., Mitchell, T.M., Healy, D., Heapet, M.J., 2006. Slip on 'weak' faults by the rotation of regional stress in the fracture damage zone. Nature 444, 922–925.

Faulkner, D.R., Mitchell, T.M., Rutter, E.H., Cembrano, J., 2008. On the structure and mechanical properties of large strike-slip faults. In: Wibberley, C.A.J., Kurz, W., Imber, J., Holdsworth, R.E., Collettini, C. (Eds.), Structure of fault zones: implications for mechanical and fluid–flow properties. Geological Society, London, Special Publications, 299, pp. 139–150.

Faulkner, D., Jackson, C., Lunn, R., Schlische, R., Shipton, Z., Wibberley, C., Withjack, M., 2010. A review of recent developments concerning the structure, mechanics and fluid flow properties of fault zones. J. Struct. Geol. 32, 1557–1575.

Goddard, J.V., Evans, J.P., 1995. Chemical changes and fluid–rock interaction in faults of crystalline thrust sheets, northwestern Wyoming, U.S.A. J. Struct. Geol. 17, 533–547.

Gonzalez, G., Niemeyer, H., 2005. Cartas Antofagasta y Punta Tetas, Región Antofagasta. Servicio Nacional de Geología y Minería, Carta Geológica de Chile, Serie Geología Básica 89: 35, escala 1:100.000.

Gonzalez, G., Dunai, T., Carrizo, D., Allmendinger, R., 2006. Young displacements on the Atacama Fault System, Northern Chile from field observations and cosmogenic ^{21}Ne concentrations. Tectonics 25. http://dx.doi.org/10.1029/2005TC001846 (TC3006).

Grant, J.A., 1986. The isocon diagram —a simple solution to Gresens' equation to metasomatic alteration. Econ. Geol. 81, 1976–1982.

Grant, J.A., 2005. Isocon analysis: a brief review of the method and applications. Phys. Chem. Earth 30, 997–1004.

Gresens, R.L., 1967. Composition–volume relationships of metasomatism. Chem. Geol. 2, 47–55.

Grocott, J., Brown, M., Dallmeyer, R.D., Taylor, G.K., Treloar, P.J., 1994. Mechanisms of continental growth in extensional arcs: an example from the Andean plate–boundary zone. Geology 22, 391–394.

Hammond, K.J., Evans, J.P., 2003. Geochemistry, mineralization, structure, and permeability of a normal fault zone, Casino mine, Alligator Ridge district, north central Nevada. J. Struct. Geol. 25, 717–736.

Hashimoto, Y., Nikaizo, A., Kimura, G., 2009. A geochemical estimation of fluid flux and permeability for a fault zone in Mugi mélange, the Cretaceous Shimanto Belt, SW Japan. J. Struct. Geol. 31, 208–214.

Herrera, V., Cembrano, J., Olivares, V., Kojima, S., Arancibia, G., 2005. Precipitación por despresurización y ebullición en vetas hospedadas en un dúplex de rumbo extensional: evidencias microestructurales y microtermométricas. Rev. Geol. Chile 32, 207–228.

Hippertt, J.F., 1998. Breakdown of feldspar, volume gain and lateral mass transfer during mylonitization of granitoid in a low metamorphic grade shear zone. J. Struct. Geol. 20, 175–193.

Holdsworth, R.E., 2004. Weak faults — rotten cores. Science 303, 181–182.

Jensen, E., Cembrano, J., Faulkner, D., Veloso, E., Arancibia, G., 2011. Development of a self-similar strike-slip duplex system in the Atacama Fault System, Chile. J. Struct. Geol. 33, 1611–1626.

Jowett, E., 1991. Fitting iron and magnesium into the hydrothermal chlorite geothermometer. GAC/MAC/SEG Joint Annual Meeting, Toronto. , 16, p. A62.

Kranidiotis, P., MacLean, W.H., 1987. Systematics of chlorite alteration at the Phelps Dodge massive sulfide deposit. Matagami, Quebec. Econ. Geol. 82, 1898–1991.

Kwon, S., Park, Y., Park, C., Kim, H.S., 2009. Mass-balance analysis of bulk-rock chemical changes during mylonitization of a megacryst-bearing granitoid, Cheongsan shear zone, Korea. J. Asian Earth Sci. 35, 489–501.

Lopez-Moro, F.J., 2012. EASYGRESGRANT — a Microsoft Excel spreadsheet to quantify volume changes and to perform mass-balance modeling in metasomatic systems. Comput. Geosci. 39, 191–196.

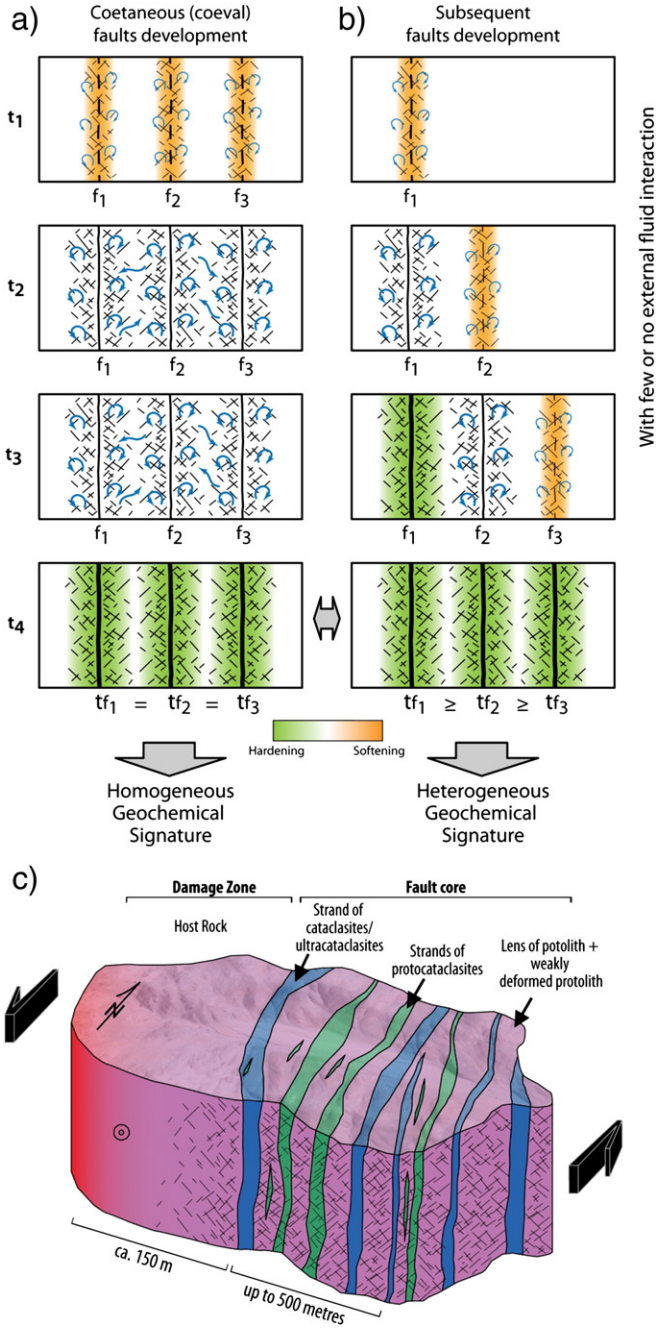

Fig. 10. Conceptual model for multiple core fault zone development. (a) Multiple fault cores from coeval fault coalescences, showing hypothetical temporal evolution from t_1 to t_4. Following this model, each rock type would present a similar geochemical behavior in terms of chemical mobility as consequence of the same fluid/rock ratio. (b) Multiple fault cores as result of amalgamation of subsequent individual faults evolving from t_1 to t_4. In this second model, geochemical dispersion and variability observed between rocks with similar deformational characteristics but belonging to different evolution stages would be explained because of different fluid/rock interaction rates existing in every deformational stage. (c) Conceptual model for the hydrothermal alteration related to fault development and chemical mobility for the Caleta Coloso Fault.

Miller, S.A., Nur, A., Olgaard, D.L., 1996. Earthquakes as a coupled shear stress high pore pressure dynamical system. Geophys. Res. Lett. 23, 197–200.
Miller, S.A., Collettini, C., Chiaraluce, L., Cocco, M., Barchi, M., Kaus, B.J.P., 2004. Aftershocks driven by a high-pressure CO_2 source at depth. Nature 427, 724–727.
Mitchell, T.M., Faulkner, D.R., 2009. The nature and origin of off-fault damage surrounding strike-slip fault zones with a wide range of displacements: a field study from the Atacama Fault System, Northern Chile. J. Struct. Geol. 31, 802–816.
Mitchell, T.M., Faulkner, D.R., 2012. Towards quantifying the matrix permeability of fault damage zones in low porosity rocks. Earth Planet. Sci. Lett. 339–340, 24–31.
Miyahara, M., Kitagawa, R., Uehara, S., 2005. Chlorite in metabasites from the Mikabu and North Chichibu belts, Southwest Japan. Clay Clay Miner. 53, 466–477.
Morton, M., Girty, G.H., Rockwell, T.K., 2012. Fault zone architecture of the San Jacinto Fault zone in Horse Canyon, southern California: a model for focused post-seismic fluid flow and heat transfer in the shallow crust. Earth Planet. Sci. Lett. 329–330, 71–83.
Naranjo, J., 1987. Interpretación de la actividad cenozoica superior a lo largo de la Zona de Falla de Atacama, norte de Chile. Rev. Geol. Chile 31, 43–55.
O'Hara, K., 1988. Fluid–flow and volume loss during phyllonitization —an origin for phyllonite in an overthrust setting North Carolina, USA. Tectonophysics 156, 21–36.
O'Hara, K., Blackburn, W.H., 1989. Volume-loss model for trace elements enrichments in mylonites. Geology 17, 21–36.
Olivares, V., Cembrano, J., Arancibia, G., Reyes, N., Herrera, V., Faulkner, D., 2010. Significado tectónico y migración de fluidos hidrotermales en una red de fallas y vetas de un Dúplex de rumbo: un ejemplo del Sistema de Falla de Atacama. Andean Geol. 37, 473–497.
Potdevin, J.L., 1993. Gresens 92: a simple Macintosh program of the Gresens method. Comput. Geosci. 19, 1229–1238.
Scheuber, E., Andriessen, P.M., 1990. The kinematics significance of the Atacama Fault Zone, northern, Chile. J. Struct. Geol. 21, 243–257.
Scheuber, E., Gonzalez, G., 1999. Tectonics of the Jurassic–Early Cretaceous magmatic arc of the north Chilean Coastal Cordillera (22°–26°S): a story of crustal deformation along a convergent plate boundary. Tectonics 18, 895–910.
Schmidt, M.W., 1992. Amphibole composition in tonalite as a function of pressure: an experimental calibration of the Al–In-hornblende barometer. Contrib. Mineral. Petrol. 110, 304–310.
Selverstone, J., Morteani, G., Staude, J.M., 1991. Fluid channelling during ductile shearing: transformation of granodiorite into aluminous schist in the Tauern Window, Eastern Alps. J. Metamorph. Geol. 9, 419–431.
Steyrer, H., Sturm, R., 2002. Stability of zircon in a low-grade ultramylonite and its utility for chemical mass balancing: the shear zone at Mieville, Switzerland. Chem. Geol. 187, 1–19.
Sturm, R., 2003. SHEARCALC —a computer program for the calculation of volume change and mass transfer in a ductile shear zone. Comput. Geosci. 29, 961–969.
Zhang, S.Q., Tullis, T.E., 1998. The effect of fault slip on permeability and permeability anisotropy in quartz gouge. Tectonophysics 295, 41–52.
Zhang, S., Tullis, T.E., Scruggs, V.J., 1999. Permeability anisotropy and pressure dependency of permeability in experimentally sheared gouge materials. J. Struct. Geol. 21, 795–806.